Characterization of Proton and Sulfur Implanted GaSb Photovoltaics and Materials

Ebrahim Karimi

Thesis submitted to the faculty of the Virginia Polytechnic Institute and State University
in partial fulfillment of the requirements for the degree of

Master of Science
In
Electrical Engineering

Luke F. Lester, Chair
Mantu K. Hudait
Xiaoting Jia

December 9, 2020
Blacksburg, VA

Keywords: GaSb, Sulfur implantation, Proton implantation, Photovoltaics,

Characterization of Proton and Sulfur Implanted GaSb Photovoltaics and Materials

Ebrahim Karimi

ABSTRACT

III-V compound Gallium Antimonide (GaSb), with a low bandgap of 0.72 eV at room temperature, is an attractive candidate for a variety of potential applications in optoelectronic devices. Ion implantation, among non-epitaxial methods, is a common and reliable doping technique to achieve local doping and obtain high-performance ohmic contacts in order to form a pn junction in such devices. An advantage of this technique over the diffusion method is the ability to perform a low-temperature process leading to accurate control of the dopant profile and avoiding Sb evaporation from GaSb surface occurring at 370 °C.

In this work, the effect of protons and sulfur ions as two implant species on the electrical behavior of MBE-grown undoped GaSb on semi-insulating (SI) GaAs was investigated via the Hall Effect. Protons and sulfur ions were implanted at room temperature (27 °C) and 200 °C, respectively, and rapid thermal annealing (RTA) was implemented at various temperatures and durations upon encapsulated GaSb. The damage induced by protons enhanced the hole density of GaSb up to around 10 times, whereas mobilities showed both increase and decrease compared to the un-implanted one, depending on the dose. While the activation of sulfur donors at an elevated temperature was anticipated after annealing sulfur implanted GaSb, instead it led to increase in p-type concentration, as the residual damage originated from sulfur implantation dominated substitutional doping.

Furthermore, GaSb p/n photovoltaic devices were fabricated by applying sulfur implantation through silicon nitride layer at RT into an n-GaSb wafer (n-type base, p-type emitter). The device showed a rectifying current and photovoltaic characteristic. The J-V plot under AM1.5G

illumination conditions, before and after an etch-back optimizing process, indicated lower short circuit current density J_{sc}, the same open circuit voltage V_{oc}, and higher fill factor FF, compared to the photovoltaic device with a p-type base. Also, both normalized series R_s and shunt R_p resistances in p/n diode indicated lower and higher values, respectively, as opposed to a GaSb p++/p diode, indicative of higher quality and lower manufacturing defects.

Characterization of Proton and Sulfur Implanted GaSb Photovoltaics and Materials

Ebrahim Karimi

GENERAL AUDIENCE ABSTRACT

Generally, the photovoltaic effect is a process by which voltage or electric current is generated in a photovoltaic cell when exposed to light. A solar cell is a photovoltaic device, typically consisting a pn junction, that converts incident photon power into electrical power and delivered to a load to do electrical work for variety of applications. There are variety of methods to form a pn junction and fabricate such devices, among which ion implantation is a reliable doping technique. In this process, dopant ions are accelerated and smashed into a perfect semiconductor lattice, creating a cascade of damage that may displace a thousand atoms for each implanted ion and become activated after an annealing process. The ions themselves can act as either electron donors, make the semiconductor n-type, or electron acceptors, make it p-type.

In this work, sulfur ions and protons, as two implant species, were implanted into separate Gallium Antimonide (GaSb) substrates and the effect of each on the electrical behavior of GaSb was investigated by Hall effect experiment. Both species raised hole carrier concentration. This behavior was not expected for sulfur ions as they would be assumed to act as electron donors after activation and convert the GaSb surface to an n-type semiconductor. It was identified that this behavior is due to the domination of created defects during implantation over the number of activated sulfur donors. The same characteristics were predicted and verified for proton implantation as well, the effect of which is just leaving damage in the lattice.

Furthermore, to verify this method for converting n-type GaSb to p-type and fabricating a pn junction in GaSb for photovoltaic application, sulfur implantation into an n-type GaSb wafer was performed and optimized by removing the excess surface damage away from the device's metal

contacts using wet etching. The device showed a diode-like rectifying current and photovoltaic characteristic. Some parameters such as short circuit current density J_{sc}, open circuit voltage V_{oc}, fill factor FF, and resistances (shunt and series) were measured and calculated using J-V plot under dark and illuminated conditions.

To my beloved wife, **Maryam**, and my beautiful daughter, **Bahar**

Acknowledgments

I would like to thank my advisor, Prof. Luke Lester, for his trust in me, valuable advice and supports, and great encouragement throughout this work. Dr. Lester not only provided me the opportunity of joining the Optoelectronics group to have a new experience in an engineering environment as an MS student, but also his words were always energizing, motivating, and confidence-boosting. Apart from his scientific knowledge in advanced material science, it is not an exaggeration to saying, Dr. Lester has taught me a lot with his personality and behavior.

I would like to acknowledge my committee members, Dr. Manto Hudait and Dr. Xiaoting Jia, for their agreeing to be members of my MS advisory committee and participate in my thesis defense; Especially Dr. Hudait for providing ADSEL measurement tools. In this regard, I would especially like to thank Dr. Michael Clavel for assisting me with measurements that played a key role in advancing this work.

I am deeply grateful to Dr. Daniel Herrera for devoting his time to train me, constantly sharing his experiences, patiently answering my questions, and clearing my mind of confusion. Undoubtedly, his experience-based contributions to my project were so useful.

Thank you to all people whose presence and activities in the Micro & Nano Fabrication Laboratory played an undeniable role in this work, especially Don Leber, who trained me for a lot of cleanroom equipment and measurement tools. His presence in his office was always encouraging and his patience in resolving issues was exemplary. I, also, would like to thank Lawrence Decker and Mark Hollingsworth, to whom I owed for keeping cleanroom machines operational.

I would like to thank Shuvodip Bhattacharya, who helped me to learn how to work with AFM.

Most of all, I would especially express my thank to my beloved wife, Maryam, who has always been encouraging and supportive of me. Also, I am so thankful to God for having my sweet daughter, Bahar, whose smiles make our life more beautiful. I also want to eternally appreciate and thank my mother, Robab, and my father, Morteza, who love and support me and deserve much credit for guiding me through life and making me the man I am today.

Table of Contents

List of Figures

List of Tables

Chapter 1

Introduction

1.1 Gallium Antimonide; Electronic and Optoelectronic Properties

Gallium antimonide (GaSb), among compound III–V semiconductors, is an interesting material from a variety of points of view. Having lattice constant of 6.095 Å, GaSb lattice is matched with many ternary and quaternary III-V compounds such as InAsSb and AlGaSbAs, makes it to be considered as a substrate material [1].

In CMOS technology, GaSb is a potentially attractive material for p-MOSFET because of its high bulk mobility for holes (~850 cm^2/Vs), which is among the highest of all III–V semiconductors and twice as high as silicon and GaAs. The electron mobility in GaSb is five times higher, as compared with that in silicon.

GaSb has a band gap of 0.72 eV, which is well matched to the loss minima for optical fiber communication and large enough to enable a high figure of merit (FOM), as compared to other III–V semiconductors [2].

GaSb based materials have potential applications in optoelectronic devices as the optimum substrate in laser diodes [3] and photodetectors [3], [4], superlattices [6], photovoltaics [7], [8], and thermophotovoltaics cells [9]–[11]. As device applications, GaSb-based devices have a variety of applications in military and civil scenarios such as infrared (IR) imaging sensors as well as fire and environmental pollution detection since the wavelength corresponding to the bandgap of GaSb-based devices matches the wavelengths of most of industrial gases and water vapor which are in the IR range.

Undoped GaSb is naturally p-type, regardless of growth technique, because of residual acceptors related to gallium vacancies (V_{Ga}) and gallium on the antimony site (GaSb) with doubly ionized nature [2]. It is found that the hole concentrations measured at room temperature (RT) are typically in the order of 10^{16} cm^{-3} for epilayers and 10^{17} cm^{-3} for bulk materials with a mobility of 600 to 800 cm^2/Vs [12].

1.2 Ion Implantation

1.2.1 Basic Concepts

Ion implantation, among non-epitaxial techniques, is of technological importance in the preparation of doped semiconductors by impinging and penetrating energetic ions into a target surface that brings about controlled and predictable impurity depth profile and ion distribution. Ion implantation precisely introduces a specific dose or number of dopant atoms, ranging from 1×10^{11} cm^{-2} to 1×10^{18} cm^{-2}, into semiconductors by counting electrical charge on the ions based

on collection in a Faraday cup. The dose is simply controlled by adjusting implant time or beam current. The energy of the ion is the significant factor that determines the type of stopping that an ion undergoes in ion implantation.

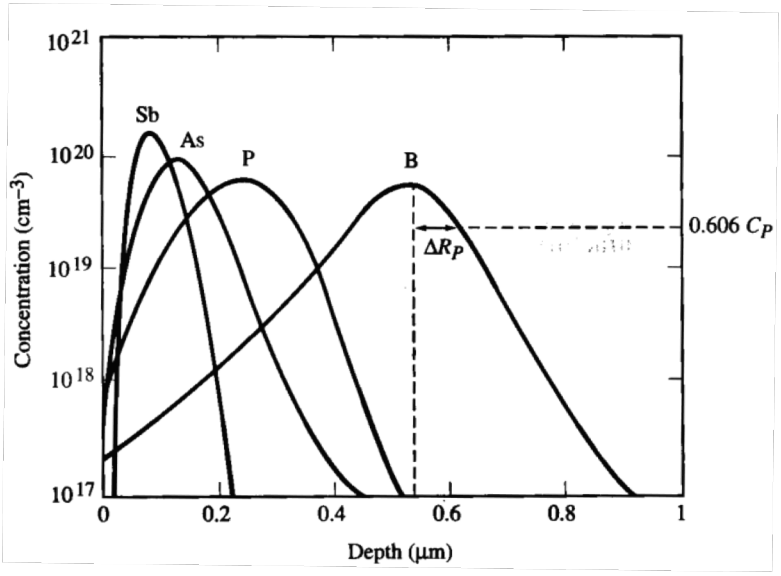

Figure 1-1: Distribution of ions implanted into crystalline silicon at an energy of 200 keV.

In terms of depth, the projected range R_p depends on the energy that is used for the implant, higher energies give deeper ranges. If different ions are implanted with the same energy, the heavy ions do not travel as far in the crystal as light ions and, so, stop at a shallower depth (Figure 1-1).

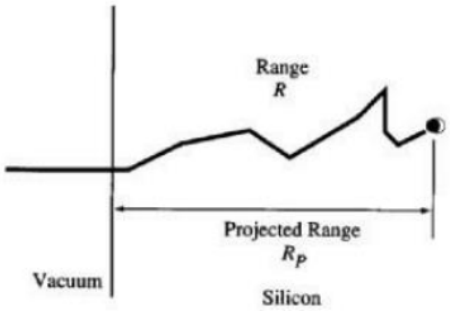

Figure 1-2: Schematic of the actual range (R) of an implanted ion and the projected range (R_p).

In spite of precision in the dose control, ion implantation is a random process as each ion follows a random trajectory with a range R and scattered off the lattice host atoms before losing its energy and coming to rest at some location, as illustrated in Figure 1-2. But, the main reason that this is a successful technique is implanting a large number of ions—ranging from 1×10^{11} cm^{-2} to 1×10^{18} cm^{-2}—and calculating an average for the distribution, peaked at a projected depth R_p, for the dopants [13].

Ion implantation offers many advantages over diffusion to introduce impurity atoms into the semiconductor's surface in modern fabrication technology. As a low-temperature process, ion implantation makes the impurity movement (prevalent in diffusion) minimal and also provides the possibility of use of a wide variety of materials such as photoresist, oxide, nitride, aluminum, and other metal films as barrier layers which add to the flexibility of process design.

In contrast to diffusion, all ionizable elements with different doses can be implanted into semiconductor wafers which mean that a much wider range of impurities and doses are reproducibly achievable in ion implantation.

In diffusion—for instance Zn diffusion that is a common p-type doping method for GaSb—the profile has a maximum concentration at the surface of substrate, while the doping profile in ion implantation has a Gaussian distribution which makes the concentration peak shift away from the surface and the projected depth more controllable [14].

1.2.2 Lattice Damage, Recovery, and Dopant Activation

In addition to the cost of the equipment, as one of the main disadvantages of ion implantation, this process inevitably damages the implanted region—in various forms of vacant lattice sites (vacancies), self-interstitial atoms (interstitials), vacancy clusters, interstitial clusters,

dopant-interstitial and dopant-vacancy clusters, and locally amorphized regions of the crystalline target (Figure 1-3)—due to knocking atoms out of the substrate lattice and a cascade of host atoms' displacements, leading to degradation of electrical and optical quality of implanted material. These induced defects during bombardment is dependent on ion mass, ion energy, ion dose, temperature of substrate during implantation, and electronic structure of the ions relative to that of host atoms.

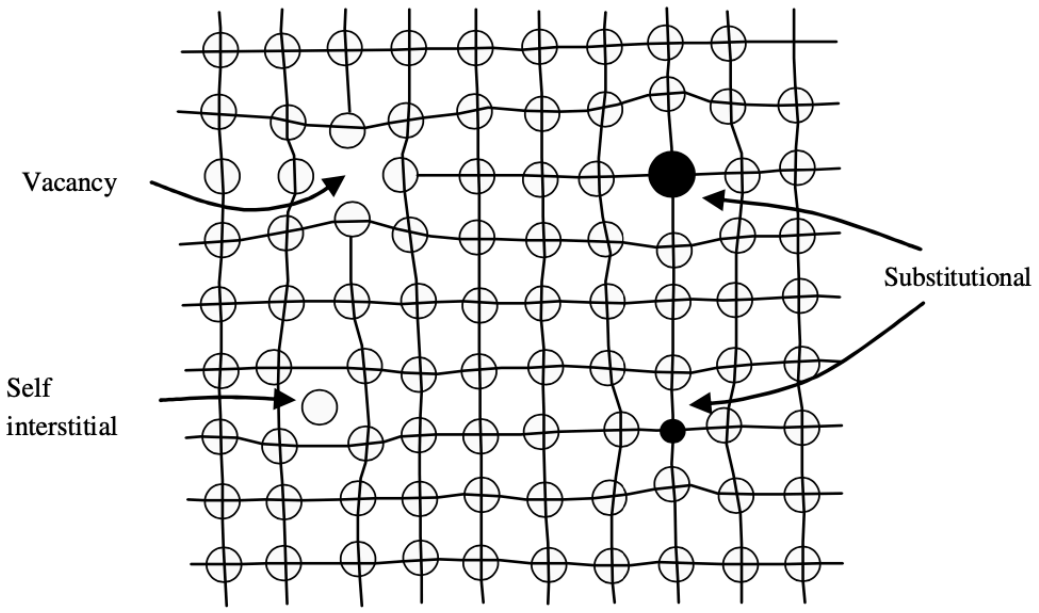

Figure 1-3: Various points defects in a simple cubic lattice [15]

For each of the ions, there is a specific dose for any target substrate above which implantation produces an amorphous layer in the implanted area that is also a function of substrate temperature. Also, amorphization depends on ion mass so that the heavier the impurity, the lower the dose required to create an amorphous layer.

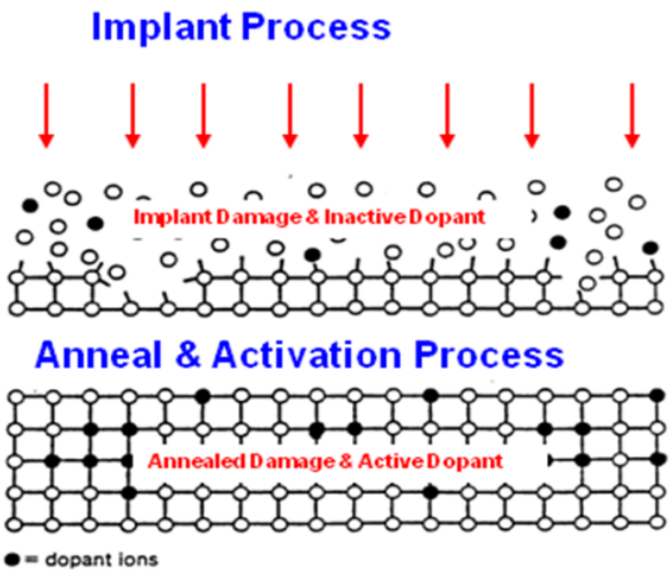

Figure 1-4: The implant damage and inactive dopant atoms left in the silicon substrate need a post implant anneal to active the dopant and recover the crystalline structure [16]

After ion implantation, a thermal process is needed for the damaged implanted target to be "annealed". In reality, thermal treatment gives rise to crystalline structure to be recovered as well as dopant atoms to be joint into the crystal lattice and electronically active (Figure 1-4). Rapid thermal processing (RTP), as the initiating solid-state processing in semiconductors, has traditionally been employed for defect annealing, recrystallization, and activation of implanted dopants. Despite having many similarities with conventional furnace annealing, RTP distinctly features much shorter processing time and rapid heating as well as cooling.

Damage removal can be divided into two different regimes: below and above amorphous threshold. At low temperatures (for instance around 400 °C for silicon) primary damage, such as di-vacancies and vacancy-type clusters, start to break up and released vacancies annihilate with interstitials and, finally, leaving only interstitial-type defects originating from extra atoms introduced into the lattice.

Restoring the crystal to its perfect state emerges for below-critical-value amounts of damage; But in damages above critical levels, arising from high-dose implantation that drive the

target amorphous, some defects shrink and some grow, turning into stable dislocation loops (secondary defects) that are much more difficult to remove. These loops are small at first and ripen to a larger mean radius after a typical RTA. In some materials such as silicon, the dislocation loops will disappear at high enough temperatures and time. In the case of amorphization, the layer-by-layer epitaxial realignment regrowth for an implanted substrate can be done using solid-phase epitaxy (SPE), a process similar to the crystallization process that occurs from a solid phase rather than liquid or gas phase.

1.3 Ion Implantation on GaSb; Advantages and Challenges

III-V compound Gallium Antimonide (GaSb), with a low bandgap of 0.72 eV at room temperature, is an attractive candidate for a variety of potential applications in optoelectronic devices [2] such as infrared photodetectors [4], [17] superlattices [6], and thermophotovoltaic (TPV) diodes [11], [18], [19]. In order to form diode junction, a selective doping is achievable using epitaxial techniques. However, it has found that growth of a GaSb pn junction can be challenging, for instance in thin molecular beam epitaxy (MBE) layers due to shunt defect formation leading to a limitation in diode area [20]. Besides, among non-epitaxial methods, ion implantation is a common and reliable doping technique to achieve local doping and obtain high-performance ohmic contacts in order to form a pn junction in such devices. Comparatively speaking, the advantage of this technique over the diffusion method is the ability to perform a low-temperature process leading to accurate control of the dopant profile and avoiding Sb evaporation from the GaSb surface occurring 370 °C. As another point, in contrast to diffusion—for instance Zn diffusion that is a common p-type doping method for GaSb—in which the profile has a maximum concentration at the surface of substrate, the doping profile in ion implantation

has a Gaussian distribution which makes the concentration peak shift away from the surface and the projected depth controllable. All of these advantages have made the ion implantation technique effective for the fabrication of GaSb-based optoelectronic devices.

However, considering unappealing aspects of this technique, using ion implantation in III-V semiconductors and particularly GaSb makes damage to the crystal structure due to a cascade of host atoms' displacements and can detrimentally have an effect on electrical and optical properties of semiconductors. About swelling, previous systematic studies on the surface elevation of some III-V compounds like GaSb and InSb show swelling of the implanted region for high ion dose and mass implantation so that, for instance, step heights of 25 nm and 6 μm has been reported by Callec et al. for Ar implanted GaSb at doses of 10^{14} cm^{-2} and 10^{16} cm^{-2} and energies of 150 keV and 250 keV, respectively [21], [22]. It means these induced defects during bombardment is dependent on ion mass, ion energy, ion dose, temperature of substrate during implantation, and electronic structure of the ions relative to that of the host atoms. Understandably, the higher the mass, the energy, and the dose of the species, the greater is the damage. Post-implantation annealing has been found as an effective way to repair induced damage, restore the crystalline quality, and electronically activate implanted atoms especially at lower doses and energies that swelling is less of a problem. However, for very high ion dosage, mass, or energy the damage becomes so great leading to amorphization as the concentration of displacements approaches the host atomic density.

Several studies for various donor and acceptor species implanted into GaSb such as Zn [23], Si [24]–[26], Be [27], [28], Ar [22], and Ne [29] have been done to investigate damage, recovery, and ions activation have been reported. In most cases, implantation with high doses has led to high radiation defects which are mainly acceptors. So, implanting n-type impurities to create

an np junction has often been so challenging as heavily damaged GaSb usually shows p-type conductivity even with donor implant; On the contrary, creating a p-type layer on n-type Gasb is much easier.

1.4 Photovoltaic Devices

1.4.1 Introduction

The photovoltaic effect—discovered by Alexander-Edmond Becquerel in 1839 in a junction formed between an electrode (platinum) and an electrolyte (silver chloride)—is a process by which voltage or electric current is generated in a cell when exposed to light.

As an example of a photovoltaic device, a solar cell consisting of a pn junction device, converts incident photon power into electrical power and delivers to a load to do electrical work for variety of applications ranging from small consumer electronics, such as a calculator, to generating power by a central power plant.

While both solar cells and photodiodes are photovoltaic devices and have similar functioning, they are qualitatively different. Unlike solar cells that are operated under bias and optimized for energy conversion efficiency, photodiodes under illumination behave as a current source, work on a narrow range of wavelengths, and are characterized under a quantum efficiency metric.

1.4.2 Solar Energy Spectrum

Figure 1-5 shows plots of incident power (spectral irradiance) emitted from the sun from the IR to the UV region—which resembles a black body radiator at a temperature of around 5700 °C—as well as the sun spectrum under two different conditions of above the earth's

atmosphere (AM0) and at the earth's surface (AM1.5). They have different measured spectra coming from atmospheric scattering and absorption effects which, therefore, depends on atmospheric composition and radiation path length through the atmosphere. These effects increase with the sun beam's path through the atmosphere.

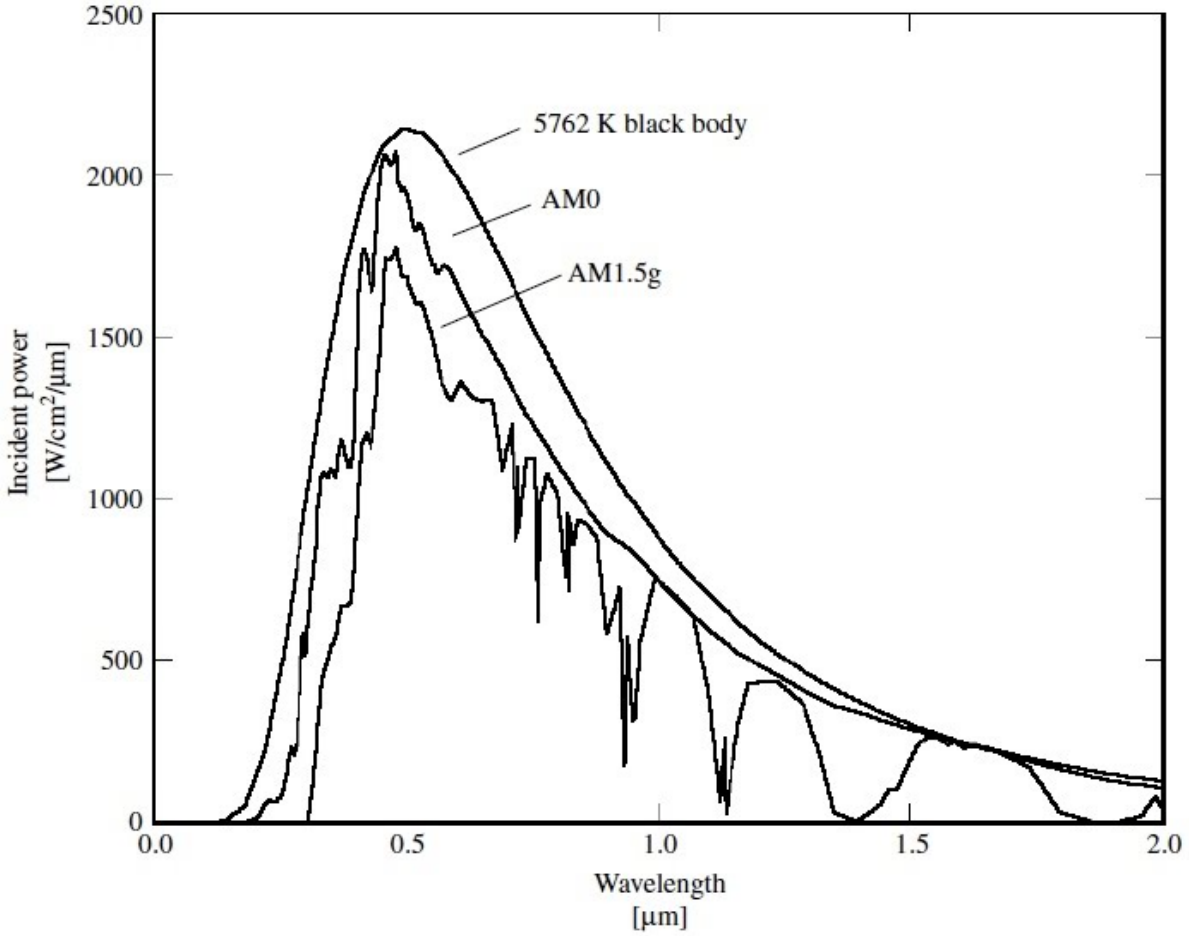

Figure 1-5: The spectrum of the solar energy vs wavelength above Earth's atmosphere (AM0) and at Earth surface (AM1.5). The black body radiation at around 5700 K is shown for comparison.

AM1 refers to the shortest path through the atmosphere, when the angle between the sun and the zenith is zero, and has an integrated power of 0.925 kW/m^2. For AM2, the angle is 60° and its intensity is 0.691 kW/m^2.

Therefore, AM1.5 is a useful representation of the atmosphere thickness as a yearly average for mid-latitudes. This air mass of 1.5 was selected as the standard spectra in the 1970s for standardization purposes based on a solar radiance analysis in the United States and represents a zenith angle of z=48.2° [30].

1.4.3 Photovoltaic Device Principles

The schematic of a photovoltaic device is shown in Figure 1-6, It includes a very narrow and heavily doped n-region as emitter—through which illumination passes—over a p-region substrate, into which the depletion region primarily extends.

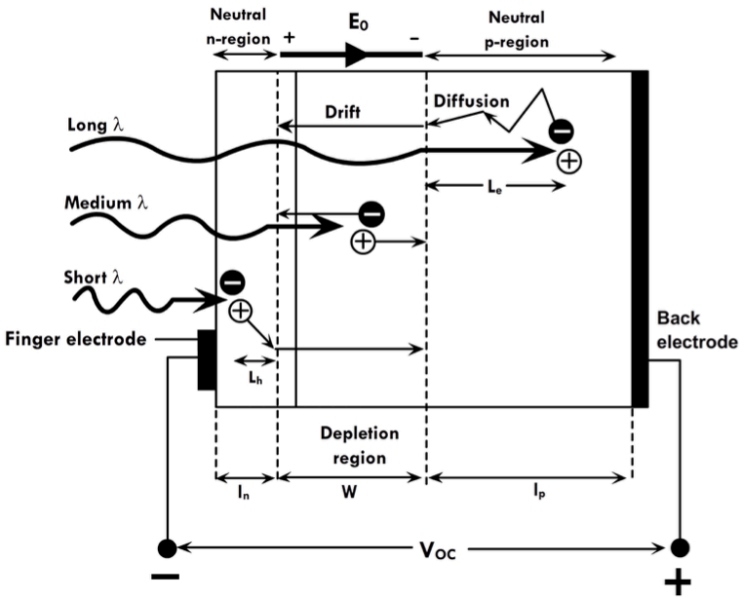

Figure 1-6: Principle of operation of a pn junction solar cell. Radiation is absorbed in the depletion region and produces electrons and holes. These are separated by the built-in potential. Depending on the wavelengths and the thicknesses different parts of the device can absorb different regions of the solar spectrum [31].

The light penetration depends on wavelengths and the absorption coefficient increases with the decrease of wavelength. The built-in potential and electric field in the depletion region are responsible for electron-hole pairs (EHPs), mainly created in the region, which makes electrons (generated in p-region) and holes (generated in n-region) drift and move to the n-region and p-region, respectively, as shown in Figure 1-6, and recombine after traveling through an external load. The shorter wavelengths (higher absorption coefficient) are generally absorbed in the emitter region (n-region) and the longer ones in the bulk p-region.

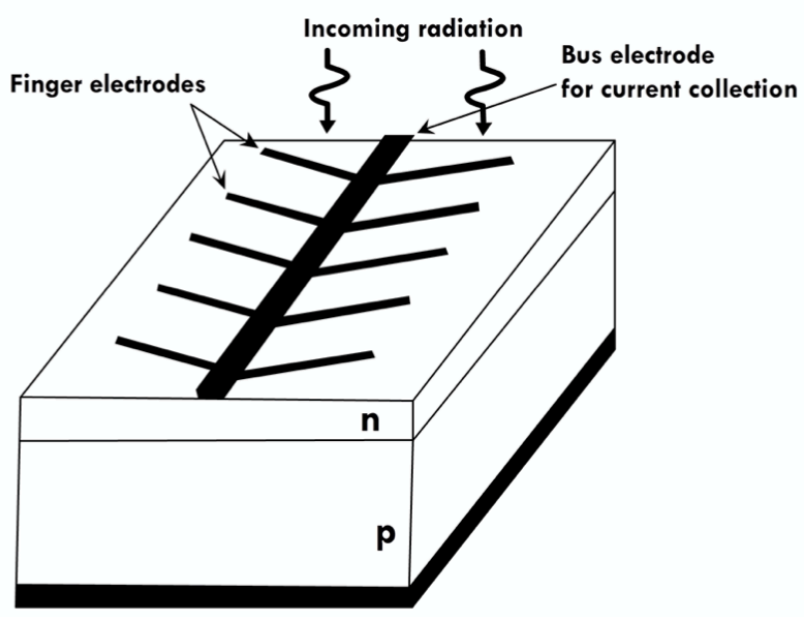

Figure 1-7: Finger electrodes on a pn junction solar cell. The design consists of a single bus electrode for carrying current and finger electrodes that are thin enough so that sufficient light can be absorbed by the solar cell [31].

The electrodes attached to the emitter side (Figure 1-7) should form an array of finger electrodes to allow illumination to enter the device and lead to small series resistance at the same time. Also, a thin antireflection coating on the surface can reduce light reflections.

1.4.4 Single-Diode Model and I-V Characteristics

A simple equivalent circuit model for a photovoltaic device consisting of a real diode in parallel with an ideal current source is shown in Figure 1-8 in which I_d and I_{ph} are the diode current and photocurrent that are opposite of each other. Also, R_s and R_p represent parasitic (series) resistance and shunt (parallel) resistance, respectively.

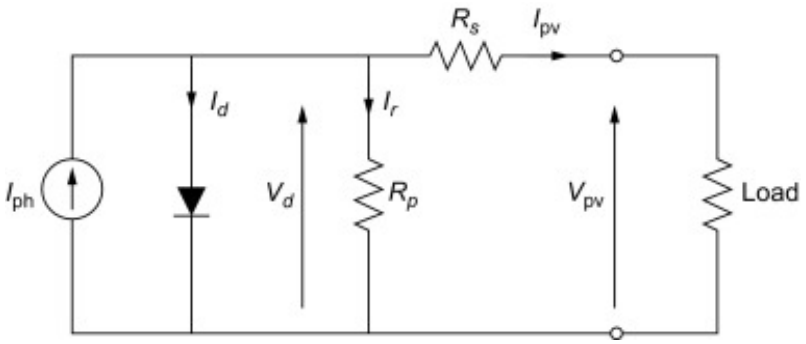

Figure 1-8: Single diode model for a general photovoltaic device [32].

When the leads of the equivalent circuit are shorted together, no current flows in the diode and, so, the whole I_{ph} flows through the shorted leads. On the other hand, if the leads are left open, the load current is null and, so, $V_{oc} = V_d$.

Based on this model, the output current of the device can be expressed as shown in the following equation:

$$I = -I_{ph} + I_0 \left(\exp\left(\frac{V - IR_s}{nV_t} \right) - 1 \right) + \frac{V - IR_s}{R_p} \qquad (1.1)$$

in which I_0 is the reverse saturation diode current, V_t is the thermal voltage of the device that is equal to $V_t = \frac{KT}{q}$ and n is the ideality factor, typically ranging between 1-2. Ideality factors higher than 2 indicates the domination of another type of current, like tunneling current.

The photocurrent I_{ph} depends on the number of EHPs photogenerated within the depletion region and the diffusion lengths L_e and L_h (Figure 1-6). The greater is the light intensity, the higher is the photogeneration rate and I_{ph}.

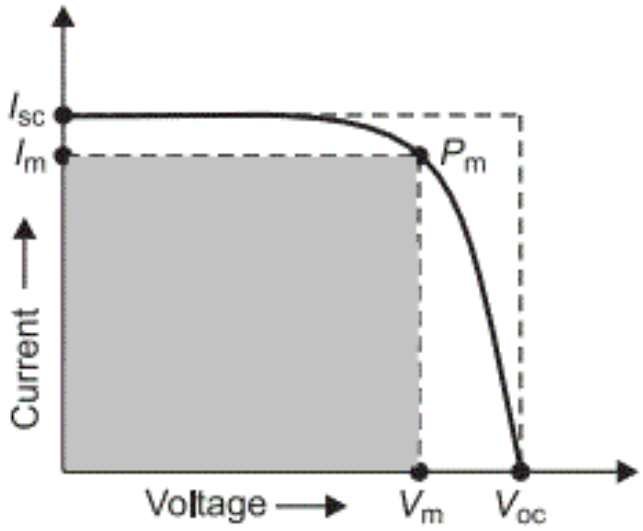

Figure 1-9: Plot of current-voltage characteristics of a generic photovoltaic device, with the maximum possible power point.

Figure 1-9 indicates a generalized I-V plot of a solar cell in which I_{sc}, V_{oc}, and $P_m(I_m V_m)$ represent the maximum possible current, the maximum possible voltage, and maximum power output. Also, the product $I_{sc}V_{oc}$ is the desired goal in power delivery for a given photovoltaic device. The fill factor of a solar cell, as a figure of merit, can be defined as:

$$FF = \frac{I_m V_m}{I_{sc} V_{oc}} \qquad (1.2)$$

In reality FF determines how close the area of shaded rectangular is to the area under the I-V curve.

Chapter 2

Fabrication Process and Measurements

2.1 SRIM/TRIM Simulation

The SRIM (Stopping Range of Ions in Matter) is a common software that is used before implantation in order to track the path of implanted ions and predict the stopping range of ions into both material stacks and single materials based on a Monte Carlo algorithm, which calculates the chain of atomic interactions in ion implantation. In SRIM, multi-element materials, like GaSb, are considered as a mixture of its constituent atoms for all material stacks. The data input and calculations of interactions are performed in TRIM, which is contained in the SRIM program and used to simulate the ion distribution of the chosen implant accelerating energies.

Inasmuch that the calculation of implanted ions is performed individually in SRIM, it is not possible to simulate a full ion implantation session and, so, a large number of ions statistically are implanted by SRIM/TRIM to predict a full implantation dose.

In order to bound surface atoms on all sides in GaSb and, so, alleviate the amount of damage after implantation, a thin layer of silicon nitride (Si_3N_4) or aluminum oxide (Al_2O_3) as protective dielectrics was applied to the surface of the substrate in most experiments in this project and added to the simulations. Table 2-1 shows all atomic parameters used for the SRIM calculations in proton and sulfur implantations into the GaSb layers.

Table 2-1: Atomic parameters relevant to the SRIM calculation of sulfur and proton implantations into GaSb substrate through Si_3N_4 and Al_2O_3 protective layers.

	S	**H**	**Ga**	**Sb**	**Si**	**N**	**Al**	**O**
Mass (amu)	32	1.008	69	121	28	14	27	16
Composition (%)	--	--	50	50	43	57	40	60
Density (g/cm3)	--	--	5.61		3.17		3.97	

2.2 Protective Film Deposition

2.2.1 PECVD Silicon Nitride Film

To bound the target (GaSb) surface atoms on all sides as well as avoid the loss of antimony and degradation of the GaSb samples during post-implant annealing, the surface of samples was covered with a layer of protective thin film.

Previous works [33] show that—under a specific recipe shown in Table 2-2 —an inert, low stress, and pinhole-free layer of silicon nitride (Si_3N_4) is achievable at a thickness of 250-260 nm and sufficiently blocks the outgassing of Sb during thermal annealing. For this purpose, in the early stages of the project, samples were sent to the Center for High Technology Materials (CHTM) at the University of New Mexico (UNM) for its ability to reliably deposit Si_3N_4 using Plasma-Enhanced Chemical Vapor Deposition (PECVD), since attempts to use the PECVD in the Whittemore cleanroom produced a high-stress film onto GaSb that easily delaminated.

Table 2-2: PECVD process parameters for 250-nm-thick Si_3N_4 layer deposition

Parameters	Value
Temperature	250 °C
N_2 pressure	15 sccm
NH_3 pressure	50 sccm
SiH_4 pressure	30 sccm
RF power	50 W
Total CVD time	22 min, 30 s

2.2.2 ALD Aluminum Oxide Film

Another experiment at Virginia Tech. that lead to an appropriate alternative for silicon nitride, including avoiding Sb out-diffusion, led to a thin layer deposition of aluminum oxide (Al_2O_3) with a thickness of 25-40 nm using atomic layer deposition (ALD) technique. This film not only is as protective as Si_3N_4 at temperatures around 600 °C in rapid thermal annealing (RTA), but also has much higher durability at temperatures up to the melting point of GaSb (712 °C) as well as higher heat processing times (performed until 30 minutes and no degradation observed).

The Al_2O_3 protection layer was deposited for some of the samples especially those needing higher temperatures/time of anneal. The ALD parameters used for this process are shown in Table 2-3.

Table 2-3: ALD process parameters for Al_2O_3 deposition

Parameters	Value
Temperature	250 °C
Flow	20 sccm
Pulse H2O	0.015 s
Wait	5 s
Pulse TMA	0.015 s
Wait	5 s
Number of cycles	200

2.3 Heat Treatment Process

In order to remove implantation-induced damages to the crystal structure provided by ion implantation as well as the activation of dopants, thermal annealing is performed—as a method for heating the substrate, holding on a specific temperature for some time, and rapidly cooling samples back to the ambient temperature—using AccuThermo AW 610 RTP system and under a nitrogen atmosphere.

In this project, heat treatment including both the rapid thermal annealing (RTA) and longer annealing times was run at a range of peak temperatures and times (from 10 seconds to 30 minutes). The profiles were designed so that, first, the temperature was slowly ramped up to 400 °C and, after keeping stabilized for a while, then was ramped up to the desired peak temperature and was finally cooled back down to the room temperature. Also, after heat treatment, the protection layer

was removed using buffer oxide etchant (BOE 10:1) which takes around 45 seconds and 30-40 minutes for Si_3N_4 and Al_2O_3, respectively. Etching of GaSb in the BOE was not significant.

2.4 Hall effect measurement

2.4.1 Background

The basic physical principle of the Hall effect—which was discovered by E. H. Hall in 1874 and used to measure the mobile carrier density and the sign of the charge carriers—is the Lorentz force, including a combination of the electric force and the magnetic force.

When an electron moves along the electric field direction perpendicular to an applied magnetic field, it experiences the magnetic force:

$$F_B = -qv \times B \qquad (2.1)$$

acting normal to both directions. The direction of this magnetic force can be determined by using the right-hand rule convention. The magnetic force direction on an electron is then determined by the opposite direction that the thumb is pointing. The resulting Lorentz force is therefore equal to:

$$F = -q(E + v \times B) \qquad (2.2)$$

The van der Pauw is a technique, used to determine the resistivity of a uniform sample, in which a thin plate sample with arbitrary shape containing four small ohmic contacts is used in order to measure the sheet resistance of R_{sh} of the sample. In reality, to determine the mobility μ

and sheet density n_s, a combination of a resistivity measurement and a Hall measurement is needed [34].

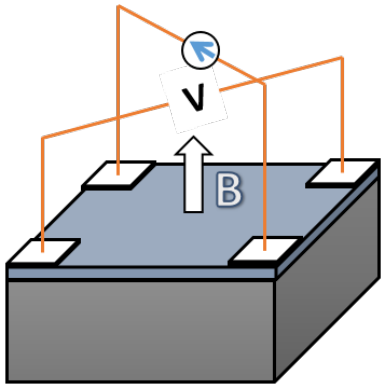

Figure 2-1: A schematic of a rectangular van der Pauw configuration for the Hall voltage measurement [35].

In order to create a typical Hall sample, deposition of 4-point contacts at the corners of the square sample is needed. It is very important to make the ohmic contacts. The Hall voltage measurement consists of a series of voltage measurements with a constant current I and magnetic field B applied perpendicular to the plane of the sample. To measure V_H, as Figure 2-1 shows, a current I is forced through the opposing pair of contacts and the Hall voltage is measured with the remaining pair of contacts. Then, the sheet density can be determine using the measured V_H and known I and B by the equation

$$n_s = \frac{IB_z}{qV_H} \qquad (2.3)$$

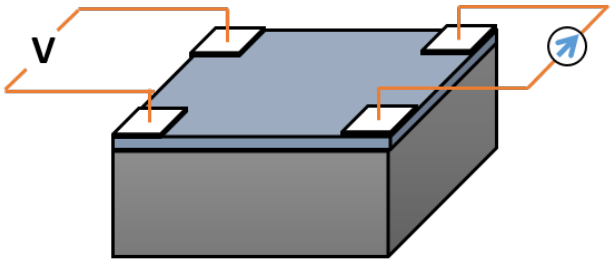

Figure 2-2: A schematic of a rectangular van der Pauw configuration for sheet resistance measurement [35]

The sheet resistance R_{sh} of the material can be conveniently determined by use of van der Pauw resistivity measurement techniques (shown in Figure 2-2), in which a dc current I is applied into two adjacent contacts (1 and 2) and the voltage across two other contacts is measured. Then the resistance (R_A) is determined by ohm's law. The same measurements should be done by applying current into contacts 2 and 3 and then the resistance R_B is calculated. R_A and R_B are related to the sheet resistance R_{sh} through the equation

$$\exp\left(-\frac{\pi R_A}{R_{sh}}\right) + \exp\left(-\frac{\pi R_B}{R_{sh}}\right) = 1 \qquad (2.4)$$

which can be numerically solved for R_{sh}.

Since sheet resistance involves both mobility and sheet density, one is able to calculate the Hall mobility through the following equation

$$\mu = \frac{|V_H|}{R_{sh} I B_z} = \frac{1}{q n_s R_{sh}} \qquad (2.5)$$

2.4.2 Hall Sample Fabrication

Unintentionally p-type GaSb with a thickness of 500 nm was epitaxially grown on a semi-insulating GaAs substrate via MBE. After SRIM/TRIM simulations, the ion implantation was performed. The purpose of using a semi-insulating (SI) substrate is to avoid leakage of current through the implanted GaSb layer. Despite the fact that the best choice for the substrate is SI-GaSb which is lattice-matched, however such substrate is not available due to lack of known impurities to make GaSb semi-insulating. The protective layer deposition process was done before/after implantation as explained in the section 2.2.

The wafer was diced using an automated dicing saw with a diamond blade into 7 mm × 7 mm pieces. Then, the annealing process and etching the protective film were done as clarified in the section 2.3. In order for cross patterning contacts, AZ nLof 2020 photoresist was painted onto the samples using a swab and soft-baked at 110 °C for 1 minute.

After removing the native oxide by dipping in HCL:H_2O solution for 30 seconds, a stack of Ti (50 nm)/Au (250 nm) was deposited as metal contacts using “the PVD-250 machine”. Then the PR layer was removed by dipping in acetone.

2.5 Photovoltaic Devices; Fabrication and Measurement

To fabricate proton and sulfur implanted GaSb photovoltaic devices, the same processes as explained in section 2.1 through 2.3 were performed.

The front metal electrode was formed via photolithography-liftoff technique for devices with side dimensions of 5 mm and 10 mm, giving device areas of 0.25 cm^2 and 1 cm^2 respectively. After coating AZ nLof 2020 photoresist onto the wafer using a spin coater and pre-exposure soft bake, the surface was exposed to a Karl Suss MA6 mask aligner system to produce the top-metal

pattern. Then, post-exposure bake, development (by AZ MIF 300), and removing native oxide—by soaking in HCl:H2O (1:3) solution—were performed. Afterwards, a stack of Pd/Ge/Au/Pt/Au was evaporated on the surface via the e-beam deposition technique using PVD-250. Then, the photoresist (PR) layer was removed by acetone and top contacts were annealed at 290 °C for 55 seconds. Also, for the back-metal contact, a stack of titanium, platinum, and gold (Ti/Pt/Au) was deposited using the PVD-250.

In order to electrically isolate devices, another PR layer was patterned via photolithography and, then, mesa wet etching was performed by soaking in an $HCl:H_2O:H_2O_2$ (50:50:1) solution for more than 3 minutes.

The J-V characteristics of photovoltaic devices were measured at room temperature (300 K) using a Unisim Compact which is a dual-zone solar simulator made by TS-Space Systems. This system includes Hydrargyrum Medium-arc Iodide (HMI) and quartz-halogen (QH) lamps which together generate a spectrum of wavelengths ranging from 320-2000 nm and was spectrally matched to the AM1.5 G solar spectrum.

In order for optimization of J-V characteristics, through removing the highly-damaged, highly-doped, highly-recombining surface between metal fingers, an etch-back process was performed by soaking in AZ400K:H2O (1:4) solution for various time durations and the J-V measurement was performed after each step. Previous works on Zn-diffused p/n GaSb [36] and sulfur-implanted p++/p GaSb photovoltaics [37] demonstrated that this process maintains the ohmic contact between the front metal contacts and the highly-doped area underneath them and makes improvement in the short circuit current density and quantum efficiency possible.

Chapter 3

Hall-Effect Characterization of Elevated-Temperature Sulfur Implanted GaSb

3.1 Introduction

Previous work on sulfur implantation into GaSb at room temperature (RT) resulted in a very high-level hole concentration, instead of acting as donors, which was attributed to the residual damage created during implantation [9].

Since ion implantation at higher temperatures—rather than RT—can be a promising method to mitigate damage during implantation and, so, raise the chance of activating sulfur donors in the GaSb lattice, this chapter is devoted to the effect of sulfur implantation at an elevated temperature on Hall effect characteristics.

3.2 Experimental

First, to determine the depth of the projected implants over a range of accelerating energies and simulate ion distributions, the Stopping and Range of Ion in Matters and Transport of Ion in Matters (SRIM/TRIM) software was used.

As Figure 3-1 shows, two sequential sulfur implantation processes were designed. Based on multiple doses and acceleration energies, the shallower implant was designed and simulated to have high doping at the surface for the ohmic contact which produces peak concentration at the depth of around 40 nm and the deeper one was chosen to have sulfur implantations at the depth of around 180 nm.

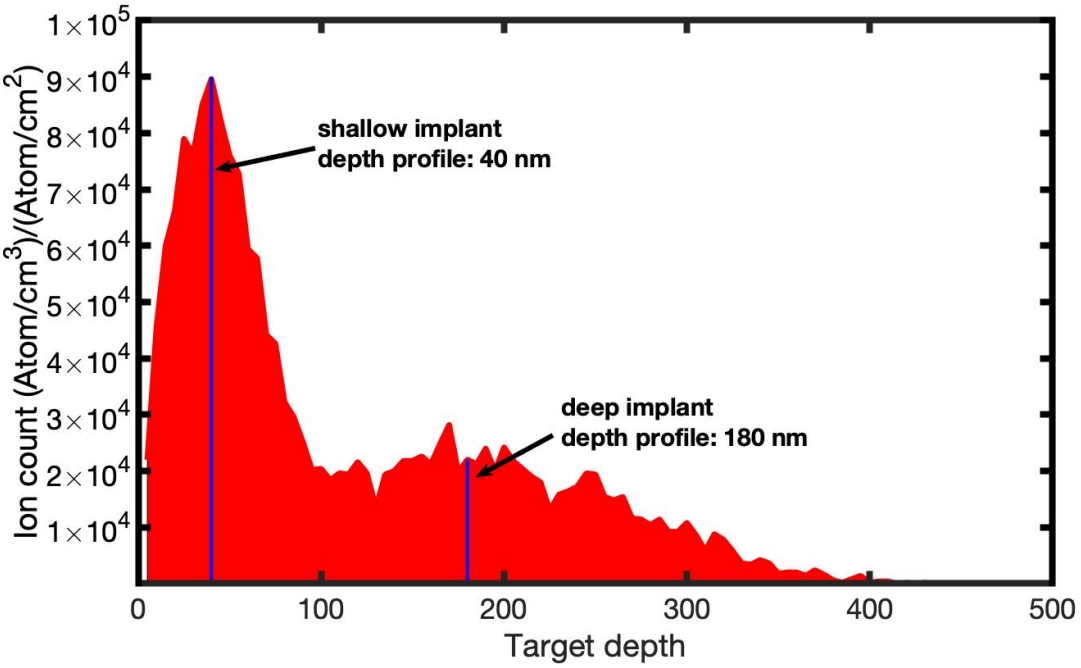

Figure 3-1: TRIM simulation of ion distribution for sulfur implantations into GaSb/SI-GaAs.

Sulfur implantation was performed at an elevated temperature of 200 °C and 7° off-axis—to minimize channeling effect—into 500 nm (100)-oriented epitaxial layers of unintentionally p-type GaSb grown by MBE on a SI-GaAs substrate.

Table 3-1: Elevated-temperature sulfur implantation conditions

Species	Multiple energy keV	Multiple dose cm^{-2}	Total dose cm^{-2}
Sulfur (S-1)	190 38	1×10^{14} 6.5×10^{13}	1.65×10^{14}
Sulfur (S-2)	190 38	3×10^{14} 1.95×10^{14}	4.95×10^{14}

Two samples with different sulfur implant dose profiles were provided based on the above-mentioned specifications. For the first one (S-1) both shallow and deep dose profiles were the same as the previous work on sulfur implanted GaSb/SI-GaAs [9]. For the second sample (S-2), the sulfur ions were implanted with tripled dose profile in order to achieve a volume concentration similar to that of Rao et al.'s work [25] in which they had successfully activated sulfur as donors for a 200 °C implant into GaSb/SI-GaAs. Table 3-1 shows details about multiple energies and doses for both sulfur implantations.

After implantation, but before annealing, a 250-nm-thick protective layer of silicon nitride (Si_3N_4) was deposited. After dicing samples, they were annealed at different temperatures ranging from 150 °C to 650 °C for different times of 10 seconds, as well as 5, 10, 15, and 30 minutes. For diced samples planned to be exposed to temperatures higher than 500 °C for more than 10 minutes, an Al_2O_3 thin film with a thickness of 25-40 nm prepared by ALD was used instead of Si_3N_4 film.

3.3 Results & Discussion

Measured by the Hall effect, the electrical characterization data of both S-1 and S-2 after 10-seconds RTA annealing at 550 °C, 600 °C, and 650 °C including sheet concentration, bulk concentration, and mobility are listed in Table 3-2. According to the results, similar to previous work sulfur implanted at RT, donor ions were not activated after annealing at any of the temperatures on both S-1 and S-2 samples, indicating the effect of damage dominates that of substitutional doping to a great degree, which leads to an increase in hole concentration above the background p-type in undoped GaSb.

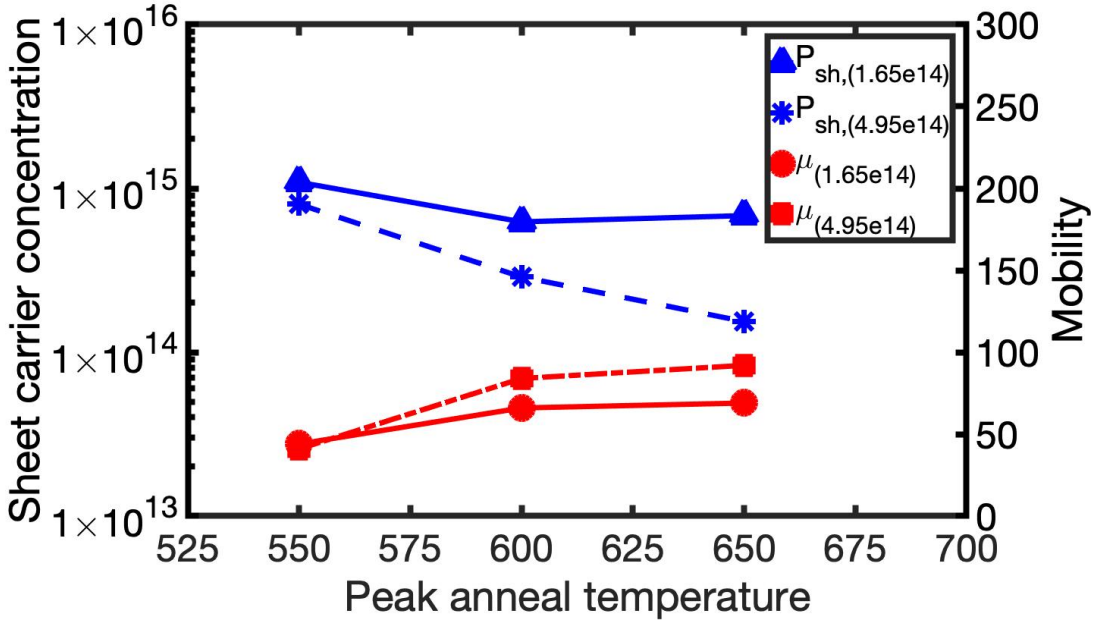

Figure 3-2: Hall measurements of sheet hole concentration and mobility vs anneal temperature (for 10 sec) for elevated-temperature sulfur-implanted MBE-grown GaSb on SI-GaAs with total doses of 1.65×10^{14} cm^{-2} and 4.95×10^{14} cm^{-2}

Table 3-2: Hall effect results of elevated-temperature sulfur-implanted GaSb on SI-GaAs before and after 10-second anneal

Sample	Anneal temperature °C	Sheet concentration cm^{-2}	Bulk concentration cm^{-3}	Mobility cm^2/Vs	Sheet density/total dose ratio
Pristine	----	8.25×10^{12}	1.65×10^{17}	255	----
S-1AI	as-implanted	8.42×10^{15}	1.68×10^{20}	8	51
S-1a	550	1.09×10^{15}	2.18×10^{19}	44	6.6
S-1b	600	6.25×10^{14}	1.25×10^{19}	66	3.8
S-1c	650	6.82×10^{14}	1.36×10^{19}	67	4.1
S-2AI	as-implanted	1.00×10^{16}	2.00×10^{20}	6	20
S-2a	550	8.00×10^{14}	1.60×10^{19}	41	1.6
S-2b	600	2.88×10^{14}	5.76×10^{18}	84	0.6
S-2c	650	2.54×10^{14}	5.09×10^{18}	92	0.5

Apart from 10-second RTA, the anneal process for longer times of 5, 10, 15, and 30 minutes was performed for both samples of S-1 and S-2 in order to make another attempt to activate donor ions.

Despite that the 200 °C elevated-temperature implant, total dose, and 5-minute annealing process were similar to Rao's work [25], which successfully activated sulfur as donors, no n-type conversion was observed for both S-1 and S-2 samples; neither for 5-minutes heat treatment, nor for extended times of 10, 15, and 30 minutes. Instead, as the Hall effect results given in Table 3.3 show, similar to 10-second RTA, longer time annealing leads to an increase in hole carrier concentration.

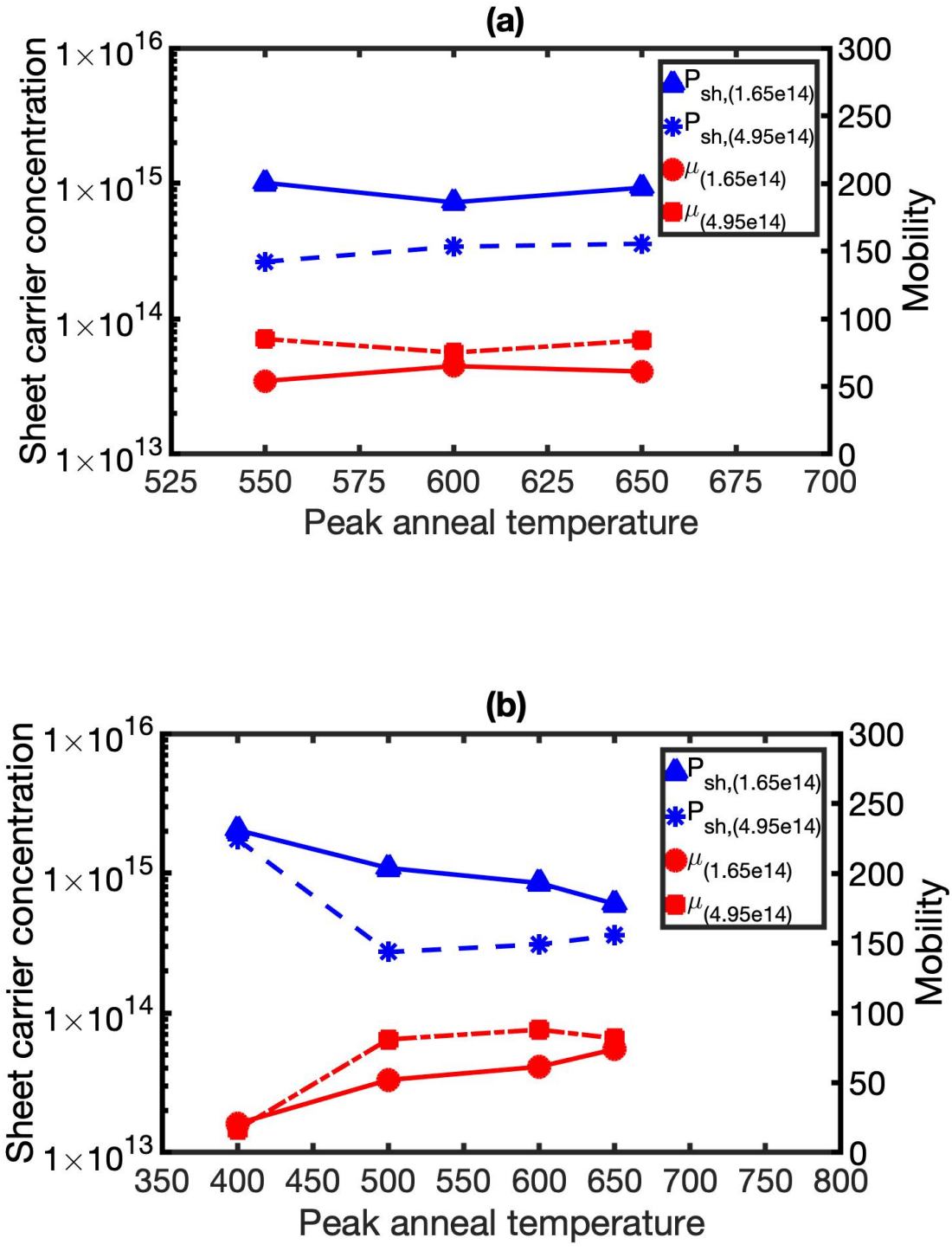

Figure 3-3: Hall measurements of sheet hole concentration and mobility vs anneal temperature for (a) 5 min; (b) 30 min for elevated-temperature S^+-implanted MBE-grown GaSb/SI-GaAs with total doses of 1.65×10^{14} cm^{-2} and 4.95×10^{14} cm^{-2}

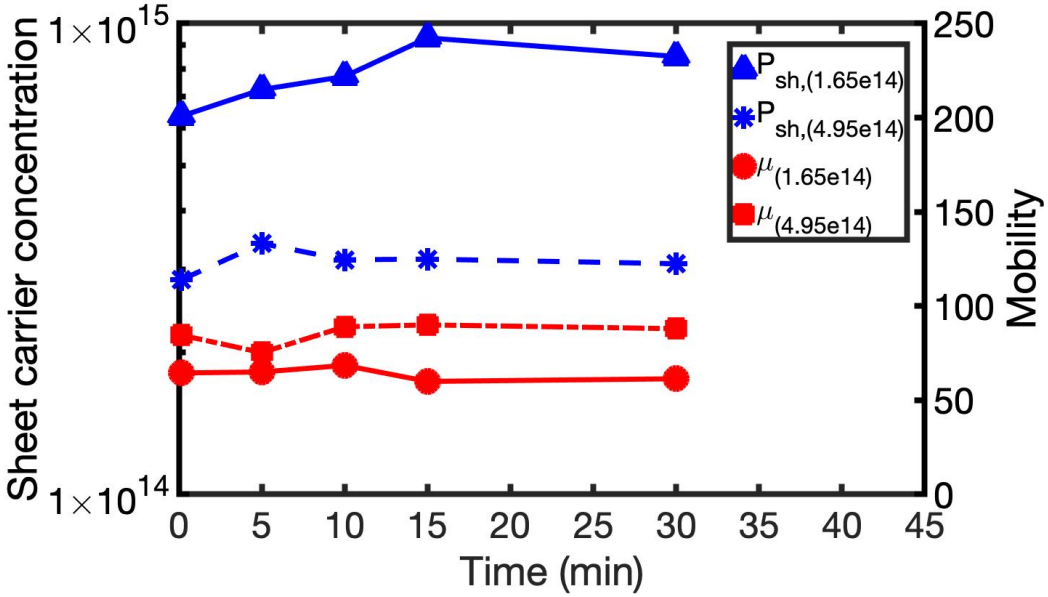

Figure 3-4: Hall measurements of sheet hole concentration and mobility vs time at peak anneal temperature of 600 °C for elevated-temperature S^+-implanted MBE-grown GaSb/SI-GaAs with total doses of 1.65×10^{14} cm^{-2} and 4.95×10^{14} cm^{-2}

Table 3-3: Hall effect results of elevated-temperature sulfur-implanted GaSb on SI-GaAs annealed at different temperatures and times

Anneal temperature °C	Anneal time	Bulk concentration cm^{-3}	Mobility cm^2/Vs	Bulk concentration cm^{-3}	Mobility cm^2/Vs
		S-1		**S-2**	
400	30 min	4.08×10^{19}	21	3.49×10^{19}	17
500	30 min	2.18×10^{19}	52	5.45×10^{18}	81
550	10 sec	2.18×10^{19}	44	1.60×10^{19}	41
	5 min	2.03×10^{19}	53	5.20×10^{18}	86
600	10 sec	1.27×10^{19}	66	5.72×10^{18}	84
	5 min	1.45×10^{19}	65	5.81×10^{18}	75
	10 min	1.64×10^{19}	69	5.31×10^{18}	89
	15 min	1.86×10^{19}	60	5.32×10^{18}	90
	30 min	1.70×10^{19}	61	5.18×10^{18}	88
650	10 sec	1.41×10^{19}	67	5.12×10^{18}	92
	5 min	1.88×10^{19}	60	7.22×10^{18}	84
	30 min	1.21×10^{19}	74	7.20×10^{18}	82

There are some explanations for this unsuccessful sulfur donor activation, one or a combination of which may have contributed. It seems that the donor activation energy is too high that these heat treatment processes do not make sulfur ions well prepared to go onto substitutional vacancies. Also, the thermal annealing may not be enough to provide the necessary energy for antimony (Sb) atoms for going out of interstitial vacancies in the crystal lattice.

Furthermore, Callec and Poudoulec have postulated an experimentally-based theory [22] for implantation into GaSb, based on which ion implantation with doses above a threshold value makes the lattice heavily damaged, formation of microtwins and voids, and swelling of implanted regions. For doses below the swelling threshold, rapid thermal annealing produces a good recovery of defects; However, for doses above, the annealing process is less efficient. During annealing, voids coalesce and are expelled toward the surface, a high density of which remain at high dose implantation and so the crystal recovery procedure is unsuccessful.

They emphasized that this swelling phenomenon should be avoided in order to obtain an almost complete recovery from the defects. From experimental and TRIM simulation results, they have estimated critical doses for some ions and established that these values correspond to a simulated number of atom displacements in the target reaching 10^{22} cm^{-3}. The Figure 3-5 shows the variation of the critical dose as a function of ion mass for implantation performed at 150 keV.

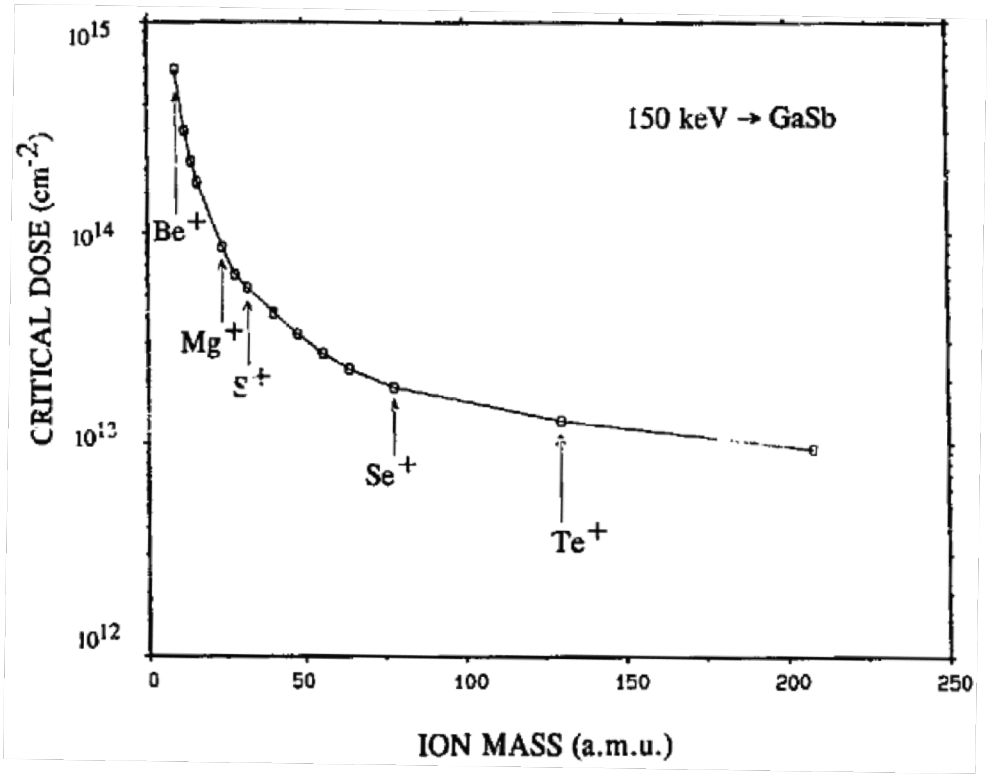

Figure 3-5: TRIM simulated variation of the critical dose (as a function of the ion mass for 150 keV), for doses above which annealing process is less efficient for crystal recovery. [22]

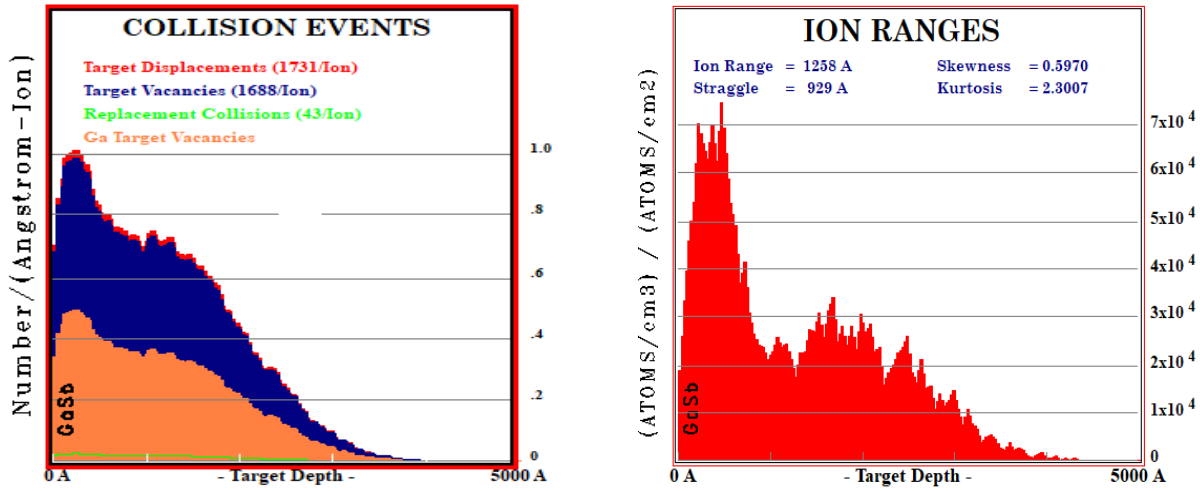

(a) **(b)**

Figure 3-6: TRIM simulation for sulfur implanted MBE-grown GaSb on SI-GaAs which shows the values of (a) target displacements per ion; (b) ion range to calculate total number of volumetric displacements.

In this project, according to this theory, the total number of volumetric displacements can be calculated using the following equation:

$$number\ of\ volumetric\ displacement = \frac{(total\ dose) \times (number\ of displacments\ per\ ion)}{ion\ range} \qquad (3.1)$$

in which ion range and number of displacements per ion are obtained by TRIM simulation (Figure 3-6)—given in TRIM simulation. Table 3-4 shows the calculated total displacements for each sulfur implanted GaSb which indicate values much more than the threshold total displacement (10^{22} cm^{-3}) predicted by Callec et al. So, this high amount of displacement would require enough energy—possibly higher than that provided by thermal annealing—to be completely recovered.

Table 3-4: Calculated total volumetric displacements for each sulfur implanted samples based on total dose, ion range, and number of displacements per ion obtained by TRIM simulation.

Sample	Total dose cm^{-2}	Ion range nm	Target displacements/ion	Total displacements/cm^3
S-1	1.65×10^{14}	126	1731	2.3×10^{22}
S-2	4.95×10^{14}			6.8×10^{22}

Moreover, all successful activation of sulfur donors implanted into GaSb are limited to just a couple of reports [25], [38]—with very low activation percentage—which is not enough to be convincing about its reproducibility and, so, presumably there is a little practical chance for it to be consistently repeatable.

From the Hall results, it is obvious from Figure 3-2 that, for both S-1 and S-2, the hole concentration and mobility, respectively, decreases and increases as the anneal temperature enhances which is contrary to the expected behavior of a substitutional doping model.

Compared to sulfur implanted at RT [9], for the sample implanted at elevated temperature with the same doses of 1.65×10^{14} cm^{-2}, no decrease in hole concentrations is observable over all anneal temperatures, rather, it increases on average. It can be concluded that, contrary to some previously reported results, sulfur implantation under the higher temperature of 200 °C is not consistently effective in mitigating the negative effects of induced damage, but actually enhanced the hole densities as a direct product of the rise in defects, which probably comes from GaSb anti-sites as a result of high-temperature implant. Numerically speaking, the measured multiplication factor between the sheet hole density and the total dose for RT-implantation work was found to be as high as 3.5 while it increased to a maximum of 6.6 after 200 °C implant.

From the point of view of comparing S-1 and S-2, in spite of the fact that the hole concentration generally decreases as temperature goes up, S-2 is showing a behavior against it in some plots (Figures 3-2 and 3-3) so that the lower dose one (S-1) has much more consistent trends. As shown by the data in Figure 3-2 and 3-3, a change in temperature or time results in less variation on average for S-2. For instance, in Figure 3-4, almost no significant change is observable in sheet hole concentration of S-2, while a relative rise in the hole concentration of S-1 is obvious.

Furthermore, comparison of hole concentrations in S-1 and S-2 reveals an interesting fact which shows the higher dose sulfur implanted samples have lower carrier densities. This result seems unexpected since damage, in this case, is considered as the only reason for the rise in hole concentration. In this regard, the first notable point is that, according to Table 3-2, although the carrier concentration of the as-implanted (un-annealed) sample with the higher dose is greater than that of the lower dose, their concentration difference is not proportional to their dose difference, not even close. In addition, it has been inversed after RTA. It seems, probably, there is a threshold

for the damage in GaSb in that the hole concentration becomes saturated and then begins to decrease.

Chapter 4

Characterization of Lattice-Damaged GaSb Using Proton Implantation

4.1 Introduction

Sulfur implantation into GaSb—whether at RT or elevated-temperature of 200 °C—was found to be so dominated by damage that this process produces p-type doping instead of n-type material.

To further investigate the effect of implant damage in GaSb, protons were chosen to show the effect of pure damage on the electrical behavior of GaSb. Protons are the smallest species to implant and, so, provided the possibility of applying a protection layer before implantation.

4.2 Hall-Effect Characterization

4.2.1 Experimental

First, to determine the depth of the projected proton implants over a range of accelerating energies and simulate ion distributions, the Stopping and Range of Ion in Matters and Transport of Ion in Matters (SRIM/TRIM) software was used.

As Figure 4-1 shows, two sequential proton implantation processes were designed. Based on multiple doses and acceleration energies, the shallower implant was designed and simulated to have high doping at the surface for the ohmic contact, which produces peak concentration at a depth of around 40 nm, and the deeper one was chosen to have proton implantations at a depth of around 180 nm.

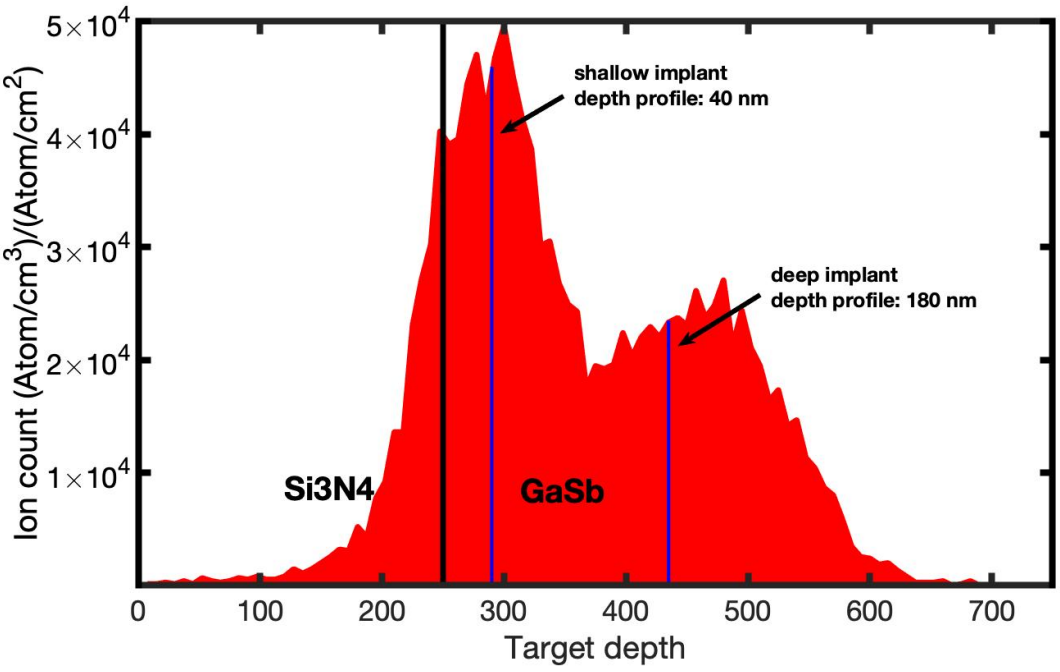

Figure 4-1: TRIM simulation of ion distribution for proton implantations into GaSb/SI-GaAs through Si_3N_4.

Proton implantation was performed at room temperature (RT) through a 250-nm-thick protective layer of silicon nitride (Si_3N_4) and 7° off-axis—to minimize the channeling effect—into 500 nm (100)-oriented epitaxial layers of unintentionally p-type GaSb grown by MBE on a SI-GaAs substrate.

Table 4-1: proton implantation conditions

Species	Multiple energy keV	Multiple dose cm^{-2}	Total dose cm^{-2}
Proton (P-1)	67 41	5×10^{13} 6.5×10^{13}	1.15×10^{14}
Proton (P-2)	67 41	5×10^{14} 6.5×10^{14}	1.15×10^{15}

Two samples with different proton implant dose profiles were performed based on the specifications given in Table 4-1. The first one (P-1) has shallow and deep dose profiles as light as 6.5e13 and 5e13 cm^{-2}, respectively. For the second sample (P-2), protons were implanted with ten times as much dose as the first one for both shallow and deep profiles.

After implantation, samples were diced and the 10-seconds RTA annealing was performed at different temperatures ranging from 575 °C to 650 °C. Finally, the silicon nitride protective layer was removed using a wet etching process that doesn't etch the GaSb significantly.

4.2.2 Results & Discussion

Table 4-2 shows the electrical data obtained by Hall measurements on annealed proton-implanted samples with different doses.

Table 4-2: Hall effect results of proton-implanted GaSb on SI-GaAs before and after 10-second anneal

Sample	Anneal temperature °C	Sheet concentration cm^{-2}	Bulk concentration cm^{-3}	Mobility cm^2/Vs
Pristine	----	8.25×10^{12}	1.65×10^{17}	255
P-1AI	as-implanted	5.98×10^{12}	1.20×10^{17}	161
P-1a	575	7.81×10^{13}	1.56×10^{18}	264
P-1b	600	3.70×10^{13}	7.40×10^{17}	267
P-1c	625	3.53×10^{13}	7.06×10^{17}	291
P-1d	650	3.25×10^{13}	6.49×10^{17}	331
P-2AI	as-implanted	3.20×10^{13}	6.40×10^{17}	141
P-2a	575	6.08×10^{13}	1.22×10^{18}	193
P-2b	600	5.54×10^{13}	1.11×10^{18}	245
P-2c	625	5.45×10^{13}	1.09×10^{18}	256
P-2d	650	6.49×10^{13}	1.30×10^{18}	231

For both samples (P-1 and P-2), the results show stronger p-type behavior, which is generally consistent with what was expected for GaSb as the proton implant leads to damage. Inasmuch as undoped GaSb is intrinsically p-type because of native defects, this result was predictable as the proton implant adds to those defects and so to carrier concentrations. However, in contrast to sulfur implants, the hole sheet density is more than 10 times lower than the dose.

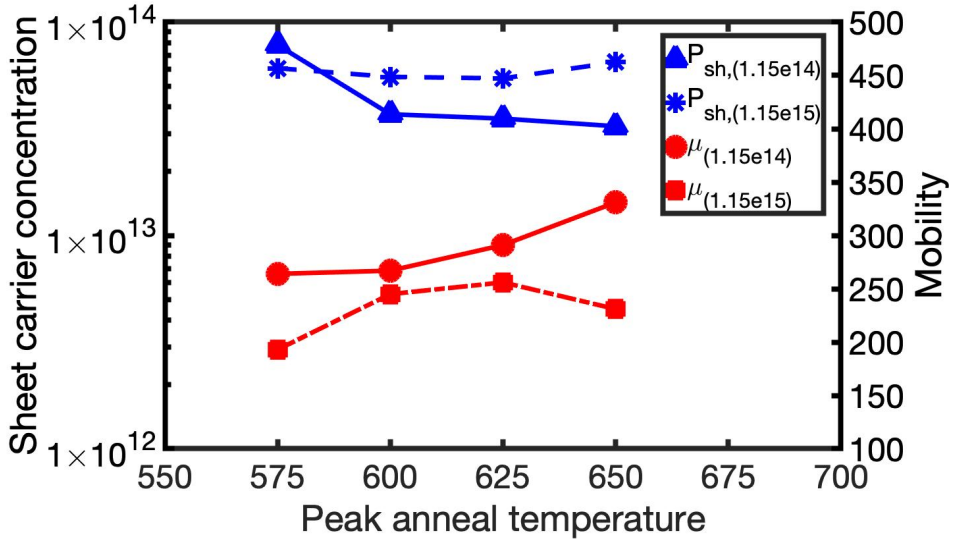

Figure 4-2: Hall measurements of sheet hole concentration and mobility vs anneal temperature (for 10 sec) for proton-implanted MBE-grown GaSb on SI-GaAs with total doses of 1.15×10^{14} cm^{-2} and 1.15×10^{15} cm^{-2}

Compared to the un-implanted GaSb with a measured bulk hole concentration of 1.65×10^{17} cm^{-3}, the proton implant improves the hole concentration by a factor in the range of 4 to 10. The highest one with 1.56×10^{18} cm^{-3} was measured for sample P-1a after 10 s rapid thermal annealing at 575 °C. Also, it is obvious that the hole concentration of P-2 samples after RTA—that is in the order of 10^{18} cm^{-3}—is on the average more than that of P-1 samples with the order of mainly 10^{17} cm^{-3}.

From the mobility point of view, annealed samples featured mobilities that differed from the pristine sample with mobility of 255 cm^2/Vs, showing 24% reduction to 30% increase so that the highest one with the hole mobility of around 331 cm^2/Vs was obtained for sample P-1 after applying 10 s RTA at 650 °C. It should be mentioned that the relatively low value of mobility in the pristine GaSb is because of threading dislocations that are due to lattice mismatch at the interface of GaSb/GaAs.

Furthermore, taking the average mobilities in the annealed samples P-1 and P-2 into account, measured mobilities in sample P-1 after RTA are more than those in sample P-2, which is probably indicative of less damage removal with increasing dosage.

The sheet concentration and mobility plots versus peak annealed temperature are shown in Figure 4-2, according to which the sheet hole concentration of both samples decreases with increasing annealing temperature because of more improvement in recovery of the damaged lattice, while the opposite trend is observed for mobility. This behavior makes sense since carriers experience more coulombic scattering in higher doping concentrations due to presence of large concentrations of ions.

4.3 Proton-Implanted GaSb Diode Performance

4.3.1 Experimental

To make a GaSb diode based on the Hall effect results of proton implantation, the implant dose and peak anneal temperature of sample P-1a (Table 4-2) was selected, because of the larger hole concentration as well as mobility compared to the pristine one.

In this fabrication process, a layer of aluminum oxide (Al_2O_3)—deposited by ALD—was used as protective layer in place of the silicon nitride. In order to determine the depth of the projected implants over a range of accelerating energies and simulate ion distributions, the Stopping and Range of Ion in Matters and Transport of Ion in Matters (SRIM/TRIM) software was used.

Proton implantation was performed at room temperature (RT) through a 40-nm-thick, pinhole-free protective layer of aluminum oxide (Al_2O_3) and 7° off-axis into a an unintentionally-doped p-type GaSb substrate. As Figure 4-3 shows, two separate protons implantation into the same undoped GaSb substrate were designed. Based on multiple doses and acceleration energies, the shallower implant was designed and simulated to have high doping at the surface for the ohmic contact which produces a peak concentration at the depth of around 35 nm with a determined dose of 6e13 cm^{-2}. The deeper implant was chosen to have a depth of around 200 nm with an implanted dose of 4.9e13 cm^{-2}. Considering the fact that the protective materials and thicknesses are different from the Hall samples, both deep and shallow doses were calculated (based on TRIM simulations) in such a way that the number of penetrated protons into GaSb was as equal as possible to that of the Hall samples.

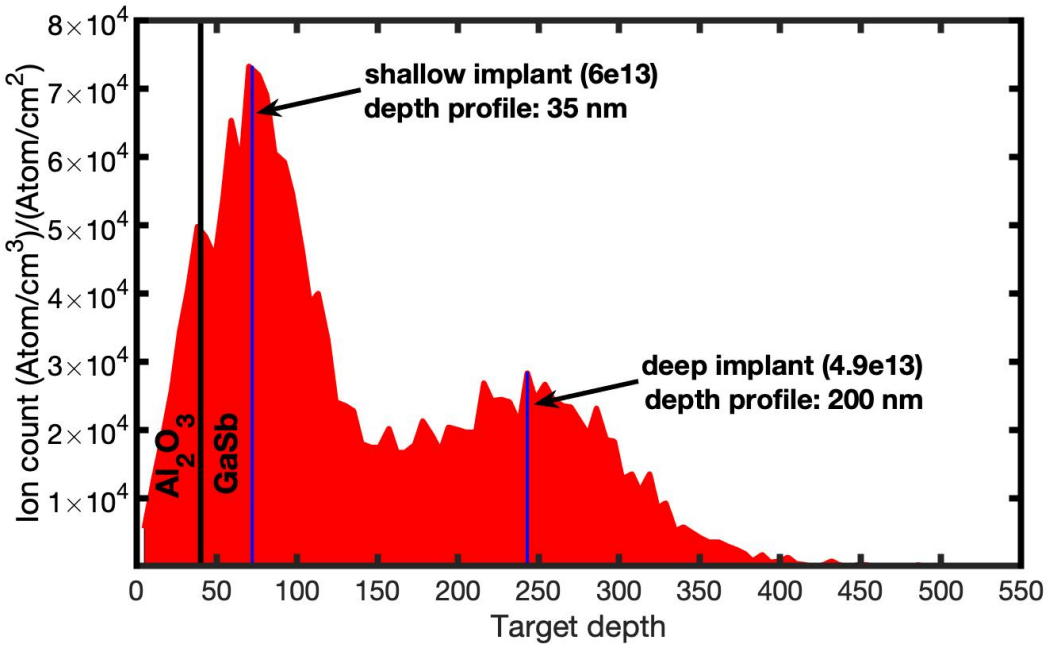

Figure 4-3: TRIM simulation of ion distribution for proton implantations into unintentionally p-type GaSb substrate through Al_2O_3.

The RTA annealing process was done for 10 seconds at a peak temperature of 575 °C in a nitrogen atmosphere. The RTA profiles were designed so that, first, the temperature was slowly ramped up to 400 °C and, after keeping stabilized for a while (60 seconds), then was ramped up to the desired peak temperature of 575 °C and was finally cooled back down to the room temperature. Then, the Al_2O_3 film was removed—using BOE 10:1 that doesn't have significant effect on GaSb—and the multi-step fabrication process including several metallizations and liftoff steps were performed, as explained in chapter 2, to make a p+/p GaSb diode with the cell areas of 0.25 and 1 cm^2.

4.3.2 Results & Discussion

The J-V characteristics of proton-implanted GaSb diode are shown in Figure 4-4. As shown, the J-V characteristics are purely ohmic that indicates no rectifying behavior, neither under dark nor under illumination. In reality, it is not a photocurrent as there is no significant difference between dark and illumination. Inasmuch as our solar simulator represents the data by "convention" (flipping the graph upside-down in solar research), increasing the voltage makes the total current of the device more negative.

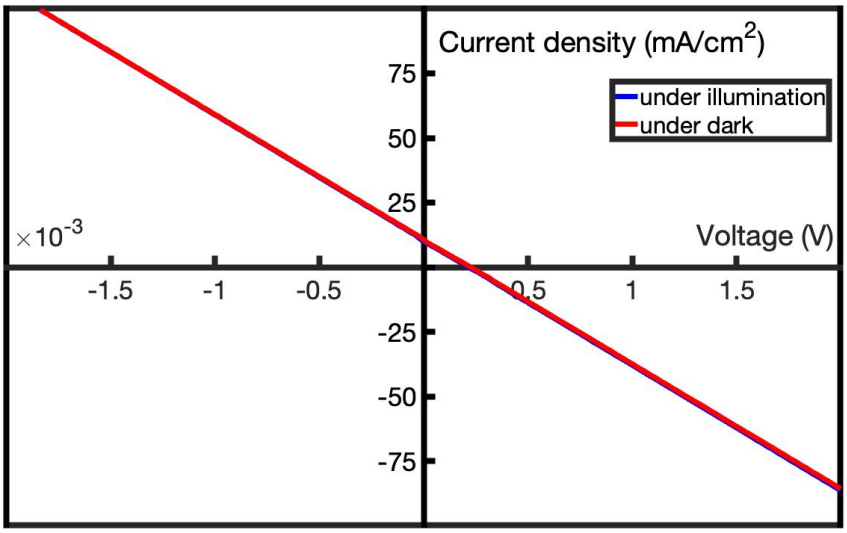

Figure 4-4: Forward and reverse-bias Characteristics of through-Al_2O_3-proton-implanted GaSb (p+/p)

Based on Hall effect results of proton implanted GaSb which showed a rise in hole concentration, this result is somewhat unexpected since a diode-like behavior was predicted for damaged-based GaSb diode like what was already observed for the sulfur-implanted GaSb p++/p photodiode [9].

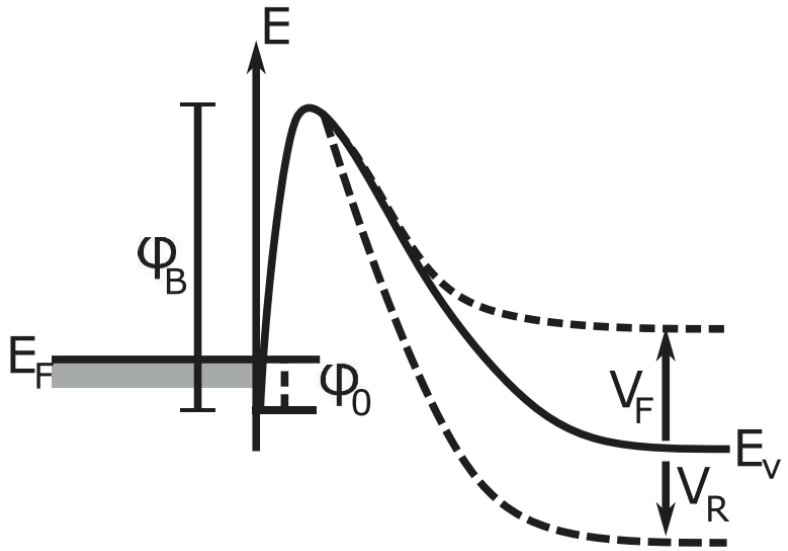

Figure 4-5: Band diagram of the metal/p++ GaSb interface [37].

In the case of a sulfur-implanted GaSb photovoltaic device, the depletion region directly beneath the front metal contacts—made by large residual damage at the surface—was responsible for the diode-like J-V characteristics. So, the shallow p++ region below the surface was responsible for inducing a built-in electric field that looks like a "hump" in the band diagram as shown in Figure 4-5 [37]. This diagram is sometimes referred to as a camel diode structure.

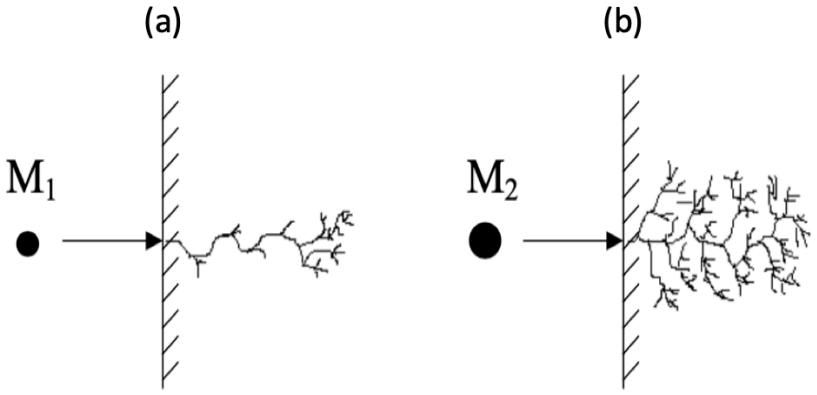

Figure 4-6: Damage tracks of implanted ions for (a) a light ion; (b) a heavy ion [39].

Since radiation damage is proportional to the ion's mass, it is understandable that light ions—like protons in this case—for which nuclear stopping becomes dominant at the end of range, leave tracks with little displacement damage (Figure 4-6 (a)); While, for sulfur as heavier ions, the tracks are more featured by displacement throughout their range and especially nearer the surface (Figure 4-6 (b)). Heavy ions, typically travel somewhat beyond their last displacement before coming to rest, which leads to a damage concentration peaked more than ion dose.

Therefore, in the proton-implanted GaSb case, it is reasonable to say that implant is distributed deeper into the materials, whereas sulfur is so much bigger and so damages the surface more. This process explains the hump in the band diagram for the sulfur implant; While the hump formed after proton implantation has presumably been very smeared out, not enough high to induce a built-in electric field below the metal contacts.

Chapter 5

Characterization of sulfur-implanted GaSb p/n photodiode

5.1 Introduction

In the previous work [9], sulfur ion implantation at room temperature (RT) has been identified as a method to provide heavy hole concentration because of the residual damage created by implantation. In an unintentionally p-type GaSb substrate, this technique was sufficient to create a diode-like p++/p rectifying photovoltaic device [37].

This chapter deals with applying this processing technique to an n-type GaSb substrate to find if damaging an n-type substrate by sulfur implantation converts it to p-type and forms a p/n

diode and, also, this p/n GaSb photodiode is characterized and compared with the sulfur implanted GaSb p++/p diode [37].

5.2 Experimental

First, to determine the depth of the projected implants over a range of accelerating energies and simulate ion distributions, the Stopping and Range of Ion in Matters and Transport of Ion in Matters (SRIM/TRIM) software was used.

Sulfur implantation was performed at room temperature (RT) through a 50-nm-thick protective layer of silicon nitride (Si_3N_4) and 7° off-axis—to minimize the channeling effect—into a tellurium-doped n-type GaSb substrate.

As Figure 5-1 shows, two separate sulfur ions implantation into the same GaSb substrate were designed. Based on multiple doses and acceleration energies, the shallower implant was designed and simulated to have high doping at the surface for the ohmic contact which produces peak concentration at the depth of around 40 nm with a determined dose of 6.5e13 cm^{-2} and the deeper implant was chosen to have a depth of around 115 nm with implanted dose of 1e14. This depth (115 nm) corresponds to the maximum accelerating energy (190 keV) which the vendor was able to achieve for implantation of singly ionized species.

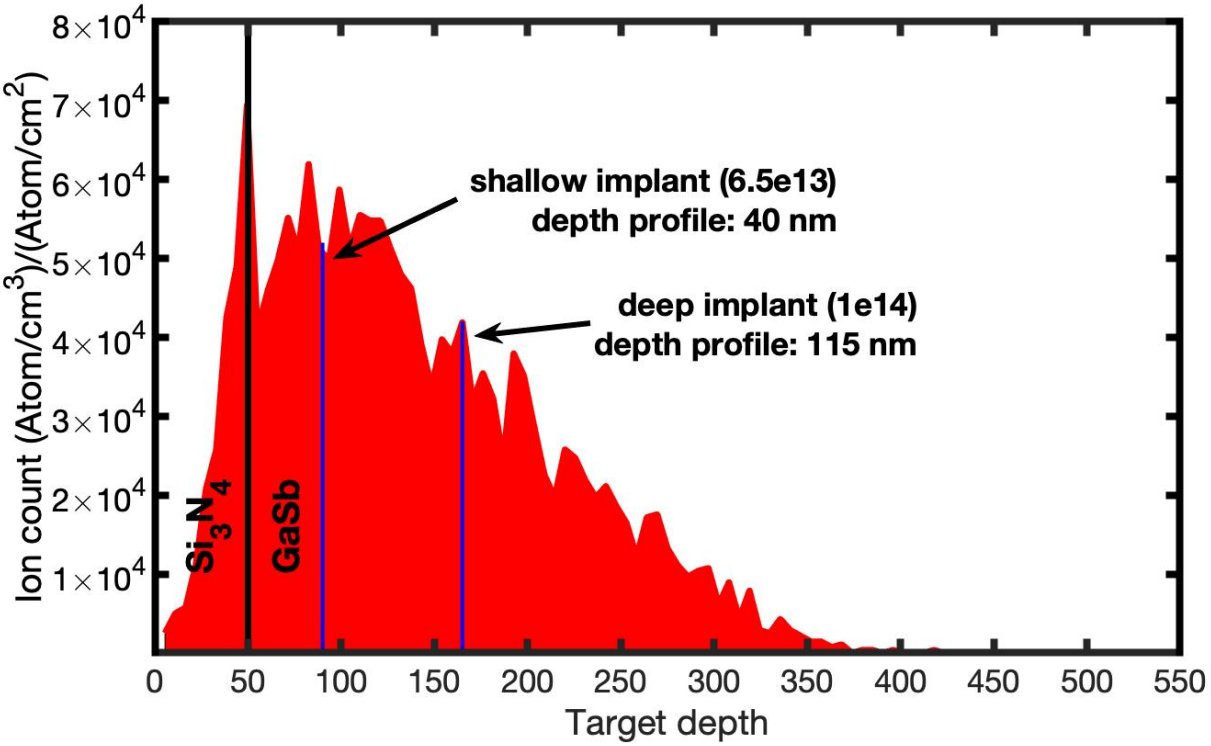

Figure 5-1: TRIM simulation of ion distribution for sulfur implantations into n-type GaSb substrate through Si_3N_4.

After implantation, an additional 200 nm Si_3N_4 film was deposited using PECVD to sufficiently protect the surface of wafer for post-implant anneal. Then, RTA annealing process was done for 10 seconds at a peak temperature of 600 °C in a nitrogen atmosphere. The RTA profiles were designed so that, first, the temperature was slowly ramped up to 400 °C and, after keeping it stabilized for a while (60 seconds), then was ramped up to the desired peak temperature of 600 °C and was finally cooled back down to the room temperature. Then, the Si_3N_4 film was removed and the multi-step fabrication process including several metallization and liftoff steps was performed, as explained in chapter 2, to make p/n GaSb diode with the cell areas of 0.25 and 1 cm^2.

5.3 Sulfur-Implanted GaSb p/n Photodiode Performance

Figure 5-2 shows the J-V plots under both dark and AM1.5 illumination. Inasmuch as around 15% of the surface area was shaded by the front metal electrode, the J-V plot indicates current density results after compensating for shading losses in the illuminated case. From the illuminated plot, a short circuit current density of 10 mA/cm^2 and an open circuit voltage of 187 mV with a fill factor of 47.8% have been measured. Also, an ideality factor of 1.56 was calculated via dark current fitting (for the logarithmic plot shown in Figure 5-3)

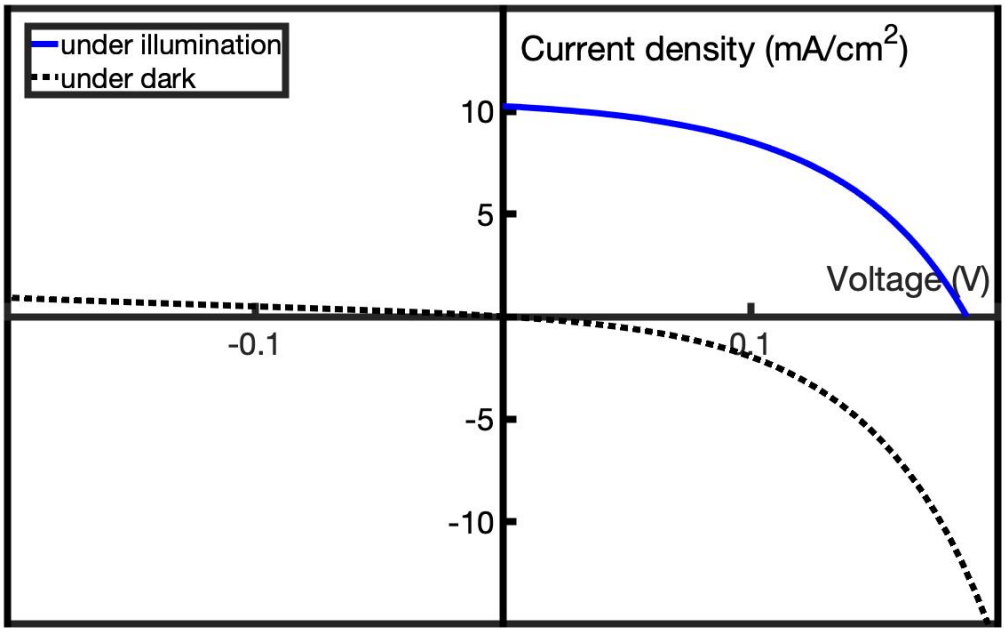

Figure 5-2: J-V measurements of sulfur-implanted GaSb p/n diode under dark (forward and reverse bias) and illumination (forward bias) conditions

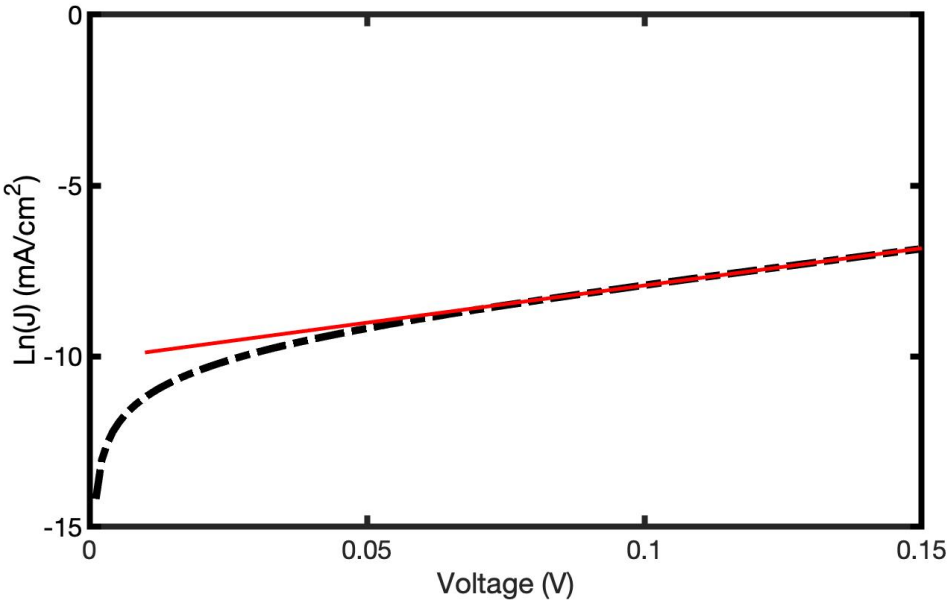

Figure 5-3: J-V measurement (log plot) of sulfur-implanted GaSb p/n diode under dark condition (forward bias) that has been used for calculating ideality factor using its slope after the voltage of V=80 mV.

As it has been previously shown, for both sulfur-implanted [9] and Zn-diffusion [36] based GaSb, the diode performance can be improved and optimized through device surface etching as shown in Figure 5-4.

It can be seen that both the short circuit current density and open circuit voltage increase with increasing etching time, so that, becoming optimized to values of 14 mA/cm^2 and 210 mV, respectively, after 120-seconds etching process. This improvement can be attributed to the effect of removing high recombination surface layers between the metal fingers which were capable of reducing the carrier lifetime.

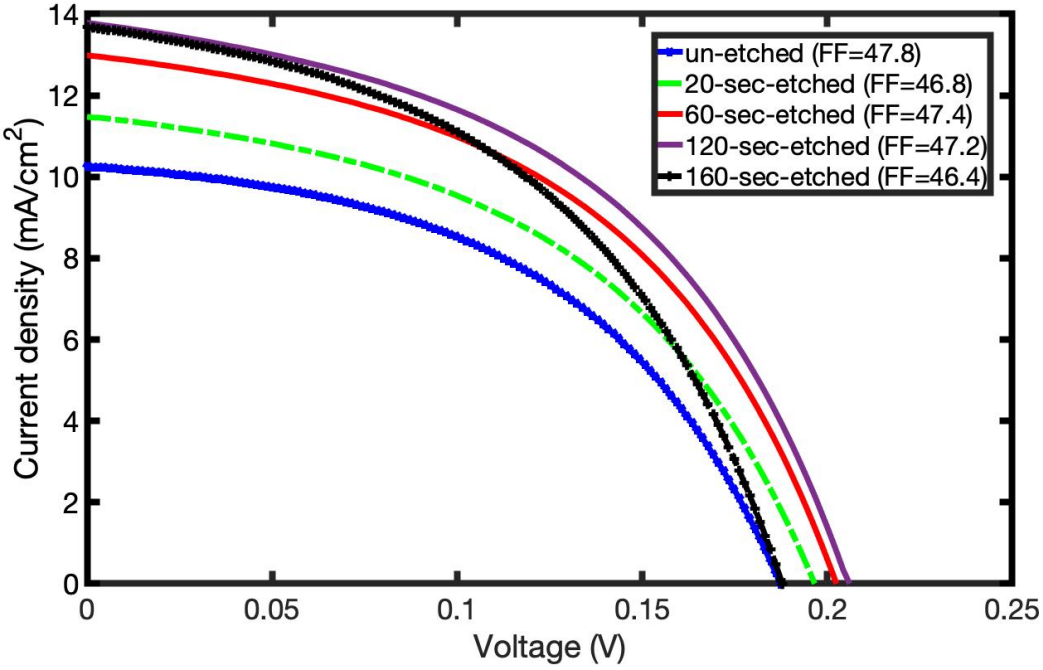

Figure 5-4: J-V characteristics of sulfur-implanted GaSb p/n diode under illumination condition as a function of etching time.

Further etching (160 seconds), did not result in improvement in the short circuit current. Rather, reduced the open circuit voltage, caused by a decrease in shunt resistance. This probably was caused by penetration of the etchant under the metal contacts which makes damage in the metal/emitter connections.

Compared to the sulfur implanted GaSb photodiode with p-type base (p++/p) [37], the optimized short circuit current density of p/n diode is lower, which obviously originates from shorter diffusion length of minority carriers (holes) in n-type GaSb substrate compared to that of minority carriers (electrons) in p-type base. Furthermore, unlike p++/p fill factor ($0.32 < FF < 0.36$), p/n diode has larger fill factor, ranging between $0.46 < FF < 0.48$ which indicates higher quality diode, coming from lower level of recombination as one of the most

essential key factors for high quality diodes. This fill factor, also, is very close to the reported fill factor (FF = 0.48) for zinc-diffusion based p/n GaSb [36].

The fill factor, as a function of open circuit voltage, is the ratio of maximum power point and $I_{sc}V_{oc}$ product and can approximately be expressed by the following equation deduced by Martin Green [40]:

$$FF = \frac{v_{m0}^2}{v_{oc}(v_{m0} + 1)} \tag{5.1}$$

in which v_{oc} and v_{m0} are the normalized open circuit and normalized maximum power point voltages, respectively, and are implicitly given by:

$$v_{0c} = \frac{qV_{oc}}{nKT} \tag{5.2}$$

$$v_{m0} = v_{oc} - ln(v_{oc} + 1) \tag{5.3}$$

which indicates a fill factor estimate based on open circuit voltage and ideality factor alone. Using (5.1) as well as experimentally measured open circuit voltage and fill factor, the ideality factor n was obtained for the p/n GaSb photovoltaic cell under AM1.5G illumination as a function of etch time, given in Table 5-1.

Unlike the sulfur implanted p++/p GaSb device that was dominated by recombination and a tunneling process, it was found that the ideality factor is significantly less than 2, $1.5 < n < 1.65$, indicative of a process intermediate between diffusion and recombination.

Table 5-1: Single-diode model parameters of sulfur-implanted GaSb p/n photovoltaic device under AM1.5G illumination.

Etch time	$V_{oc,ext}$	FF_{ext}	n	R_s	R_p	J_0	$V_{oc,int}$	FF_{int}
sec	mV	%		Ω	Ω	mA/cm^2	mV	%
0	187	47.8	1.50	6.65	524	7.63×10^{-2}	192	48.5
20	197	46.8	1.63	5.92	378	9.42×10^{-2}	205	47.9
60	202	47.4	1.62	4.92	343	8.89×10^{-2}	210	48.8
120	206	47.2	1.64	5.14	299	8.94×10^{-2}	215	49.2
160	188	46.4	1.57	4.68	293	11.41×10^{-2}	196	47.7

After obtaining ideality factor, resistance values including series resistance (R_s) and shunt (parallel) resistance (R_p) were calculated from the following expressions and given in Table 5-1:

$$R_s = \frac{dV}{dI}(@V = V_{oc}) - \frac{nK_BT}{qI_{sc}} \qquad (5.4)$$

$$R_p = \frac{dV}{dI}(@V = 0) - R_s \qquad (5.5)$$

To compare R_s and R_p of sulfur implanted-based previous work p++/p GaSb and the current work p/n GaSb, since different devices have different areas, it is reasonable to use the specific resistance ($\Omega.cm^2$) instead for the values to be normalized. The area-normalized values for the un-etched and optimized devices have been provided in Table 5-2.

Table 5-2: Normalized series and shunt resistances of the most-optimized sulfur-implanted GaSb p/n (after 120-second etching) and p++/p (after 80-second etching) photovoltaic devices.

	R_s $\Omega.cm^2$		R_p $\Omega.cm^2$	
	p++/p	**p/n**	**p++/p**	**p/n**
Un-etched	2.17	1.66	32.24	131
Most-optimized	1.42	1.28	7.92	75

From Table 5-2, both R_s and R_p values show better results in the p/n solar device compared to p++/p one. Inasmuch as the effects of the series resistance consist at high light levels in a flattening of the photovoltaic output characteristic and a related drop in the maximum power point voltage, the lower normalized series resistance of the p/n device has resulted in a higher fill factor.

Moreover, since the process flow for fabricating this sulfur-implanted GaSb p/n diode was the same as that of prior work p++/p [37] except the implantation process (this sulfur implantation was done through silicon nitride protection film unlike p++/p that was without such layer), there is a possibility for a correlation between this obvious improvement in R_p and implanting through a protection layer. Typically, the presence of a lower shunt resistance R_p is due to manufacturing defects, rather than poor solar cell design, that provide alternative current paths for the light-generated current. Also, as it was already explained, applying a dielectric film to the surface before implantation mitigates the amount of surface damage during ion implantation. So, it can be

concluded that this improvement can be mainly attributed to use of the protection layer, although it can be partly due to a larger charge differential between p and n compared to p++ and p. Anyway, determination of applying protection film contribution in this improvement definitely requires further research.

In order to obtain reverse saturation diode current I_0, both resistances can be plugged in

$$I_0 = \frac{I_{sc}(R_s + R_p) - V_{oc}}{R_p[\exp\left(\frac{qV_{oc}}{nk_BT}\right) - \exp\left(\frac{qI_{sc}R_s}{nk_BT}\right)]} \qquad (5.6)$$

Furthermore, intrinsic values can be defined for the fill factor and open circuit voltage with some assumptions. The intrinsic open circuit voltage can be obtained from photocurrent equation:

$$I_{ph} = I_0\left(\exp\left(\frac{qV_{oc}}{nk_BT}\right) - 1\right) + \frac{V_{oc}}{R_p} \qquad (5.7)$$

plugging in I_0 from equation (5.6) and assuming $\exp\left(\frac{qV_{oc}}{nkT}\right) \gg 1$ as well as an ideal R_p ($R_p = \infty$) which leads to the following expression:

$$V_{oc,int} \cong \frac{nk_BT}{q}\ln\left(\frac{I_{ph}}{I_0}\right) \qquad (5.8)$$

Also, the intrinsic fill factor can be determined using Equation (5.1) by plugging in the intrinsic open circuit voltage $V_{oc,int}$. The results of all these calculated parameters has been provided in Table 5-1 as well.

It is obvious that the relative difference between the intrinsic and extrinsic values of the fill factor in this p/n diode is much less (relatively 4% for the optimized one) than that of previous work p++/p diode (more than 20% for the optimized one) that is as a result of lower parasitic resistances. Furthermore, the fact that $V_{oc,int}$ and $V_{oc,ext}$ values are very close to each other is another result of higher shunt resistance compared to the p++/p diode.

Chapter 6

Conclusions and Future Work

6.1 Conclusions

The summary of the results of accomplishments and conclusions is as follows:

1. The Hall effect results for sulfur implantation at elevated temperature of 200 °C into 500-nm-thick GaSb—grown by MBE on SI-GaAs—indicated that the effect of residual damage originated from sulfur implantation still dominates substitutional doping so that no n-type conversion showed up at neither a 10-second RTA nor at extended annealing times up to 30 minutes at any of temperatures ranging between 400 °C-650 °C; Rather, it led to an improvement in p-type characteristics. As expected, a decreasing hole concentration and

increasing mobility as the result of an increasing anneal temperature was a general trend. Also, the results of samples with different implanted doses showed that increasing the dose results in saturation of sheet hole density at some point. Moreover, sulfur implantation at 200 °C leads to a larger ratio of sheet concentration to dose compared to that of RT implantation.

2. Making damage in GaSb lattice by proton implantation raised the hole concentration up to 10 times. This change in electrical behavior was matched with expectations as a result of damage in GaSb. Investigation of proton-implanted GaSb p+/p device showed no diode-like behavior, rather the J-V characteristics were purely resistive, which are attributed to a relatively low surface damage that is not enough to form a sharp hump at the metal/GaSb interface band diagram. Compared to implantation of bigger sulfur ions, protons deposit less damage in total and at deeper range.
3. Characterization of the GaSb p/n photovoltaic device made by using sulfur implantation at RT into an n-GaSb wafer showed a rectifying current and photovoltaic characteristic. The J-V plot under AM1.5G illumination conditions, before and after etch-back optimizing process, indicated lower short circuit current density J_{sc}—due to shorter diffusion length of minority carriers (holes) in the n-type base—the same open circuit voltage V_{oc}, and higher fill factor FF, compared to the photovoltaic device with p-type base. Also, from a resistance point of view, both normalized series R_s and shunt R_p resistances in p/n diode indicated lower and higher values, respectively, as opposed to GaSb p++/p diode, indicative of higher quality and lower manufacturing defects (presumably due to using a protection layer during implantation).

6.2 Future Work

6.2.1 Extending Depth of implanted sulfur

Compared to the literature with successful sulfur donor activation [25], this work applied the same procedure—in terms of dose and elevated temperature implant as well as extended annealing time—except for the depth profile because of our limitation in the range of accelerating energies. According to the successful work, an accelerating energy as high as 1.3 MeV is needed to implant sulfur at the depth of 1 um, doing which may potentially raise the chance of n-type conversion in GaSb. To implant in such a depth, it is required to grow thicker GaSb layer on SI-GaAs substrate.

6.2.2 Sulfur Implantation with Lower Dose

As explained in the chapter 3, according to a theory established by Callec et al. [22], implantation above a critical dose—that makes displacement of more than 10^{22} atom/cm^{-3} in the lattice—is responsible for surface swelling identified as a factor for not recovering of defects after annealing. Based on TRIM-based calculations, the value of displacements was determined at least twice the critical value. So, lower dose sulfur implantation may increase the chance for GaSb to become n-type.

6.2.3 Proton-Implanted Back Surface Field (BSF)

As one of the advantages of ion implantation over the zinc-diffusion method is the possibility of adding further implantation process steps for an existing device. A back-surface layer (BSF) can be designed to be below the base region such that carriers generated in the base are prevented from moving downwards to the substrate. This BSF would require a deep implantation into the base.

This work, introduced proton implantation as a potential option to act as an acceptor in GaSb. Since the proton is the lightest ion, it has the advantage of being deeply implanted into a p-type base GaSb diode with lower accelerating energies compared to other ions to form a deep BSF layer; Especially proton-implanted GaSb showed a mobility as high as the un-implanted one.

6.2.4 Effect of Implantation Through Dielectric Film

In this work, in the GaSb p/n device fabrication process, the sulfur implantation was introduced through a silicon nitride layer, the effect of which was reflected in the shunt resistance R_p improvement, compared to the GaSb p++/p diode.

To further investigate and determine what fraction of the R_p improvement in this project has been the result of implanting through dielectric layer, the same diode with the same specifications can be fabricated without a protective film during implantation and the R_p measurement.

References

[1] A. G. Milnes and A. Y. Polyakov, "Gallium antimonide device related properties," *Solid State Electron.*, vol. 36, no. 6, pp. 803–818, 1993, doi: 10.1016/0038-1101(93)90002-8.

[2] P. S. Dutta, H. L. Bhat, and V. Kumar, "The physics and technology of gallium antimonide: An emerging optoelectronic material," *J. Appl. Phys.*, vol. 81, no. 9, pp. 5821–5870, 1997, doi: 10.1063/1.365356.

[3] T. K. G. MOTOSUGI, "LIQUID-PHASE EPITAXIAL GROWTH AND CHARACTERIZATION OF AIGaAsSb LATTICE-MATCHED TO GaSb SUBSTRATES George," vol. 49, 1980.

[4] N. Gautam, H. S. Kim, M. N. Kutty, E. Plis, L. R. Dawson, and S. Krishna, "Performance improvement of longwave infrared photodetector based on type-II InAs/GaSb superlattices using unipolar current blocking layers," *Appl. Phys. Lett.*, vol. 96, no. 23, pp. 1–4, 2010, doi: 10.1063/1.3446967.

[5] Y. Zhang, N. Baruch, and W. I. Wang, "Normal incidence infrared photodetectors using intersubband transitions in GaSb L-valley quantum wells," *Appl. Phys. Lett.*, vol. 63, no. 8, pp. 1068–1070, 1993, doi: 10.1063/1.109835.

[6] B. Satpati, J. B. Rodriguez, A. Trampert, E. Tournié, A. Joullié, and P. Christol, "Interface analysis of InAs/GaSb superlattice grown by MBE," *J. Cryst. Growth*, 2007, doi: 10.1016/j.jcrysgro.2006.11.284.

[7] B. P. Conlon, D. J. Herrera, S. A. Abdallah, J. O. Okafor, and L. F. Lester, "Performance of GaSb Photovoltaics with Graphene Coating," 2018, doi: 10.1109/pvsc.2017.8366632.

[8] E. Vadiee *et al.*, "AlGaSb based solar cells grown on GaAs by Molecular Beam Epitaxy," in *Conference Record of the IEEE Photovoltaic Specialists Conference*, 2016, doi: 10.1109/PVSC.2016.7750050.

[9] D. J. Herrera and L. F. Lester, "Electrical and material characterization of sulfur-implanted

GaSb," *J. Vac. Sci. Technol. B*, vol. 37, no. 3, p. 031214, 2019, doi: 10.1116/1.5093329.

[10] C. A. Wang, H. K. Choi, S. L. Ransom, G. W. Charache, L. R. Danielson, and D. M. DePoy, "High-quantum-efficiency 0.5 eV GaInAsSb/GaSb thermophotovoltaic devices," *Appl. Phys. Lett.*, 1999, doi: 10.1063/1.124676.

[11] A. W. Bett and O. V. Sulima, "GaSb photovoltaic cells for applications in TPV generators," *Semicond. Sci. Technol.*, 2003, doi: 10.1088/0268-1242/18/5/307.

[12] R. D. Baxter, R. T. Bate, and F. J. Reid, "Ion-pairing between lithium and the residual acceptors in GaSb," *J. Phys. Chem. Solids*, vol. 26, no. 1, pp. 41–48, 1965, doi: 10.1016/0022-3697(65)90070-3.

[13] P. B. G. James D. Plummer, Michael D. Deal, *Silicon VLSI Technology : Fundamentals, Practice, and Modeling*. Prentice Hall, 2000.

[14] Richard C. Jaeger, *Introduction to Microelectronic Fabrication*, Second Edi. Prentice Hall, 2002.

[15] M. Nastasi and J. W. Mayer, *Ion implantation and synthesis of materials*. Springer-Verlag, 2006.

[16] M. A. B. Chang, *High Mass Molecular Ion Implantation*. Axcelis Tech. Inc., 2011.

[17] A. Dehzangi, R. McClintock, A. Haddadi, D. Wu, R. Chevallier, and M. Razeghi, "Type–II superlattices base visible/extended short–wavelength infrared photodetectors with a bandstructure–engineered photo–generated carrier extractor," *Sci. Rep.*, vol. 9, no. 1, pp. 1–7, 2019, doi: 10.1038/s41598-019-41494-6.

[18] F. Z. Meharrar, A. Belfar, I. Aouad, E. Giudicelli, Y. Cuminal, and H. Aït-kaci, "Analysis of the GaSb-p+/GaSb-p/GaSb-n+/GaSb-n structure performances at room temperature, for thermo-photovoltaic applications," *Optik (Stuttg).*, vol. 175, no. June, pp. 138–147, 2018, doi: 10.1016/j.ijleo.2018.08.125.

[19] M. Zenker and A. Heinzel, "Efficiency and power density potential of combustion-driven thermophotovoltaic systems using GaSb photovoltaic cells," *IEEE Trans. Electron Devices*, vol. 48, no. 2, pp. 367–376, 2001, doi: 10.1109/16.902740.

[20] O. S. Romero *et al.*, "Transmission electron microscopy-based analysis of electrically

conductive surface defects in large area GaSb homoepitaxial diodes grown using molecular beam epitaxy," *J. Electron. Mater.*, 2014, doi: 10.1007/s11664-014-3070-0.

[21] R. Callec, P. N. Favennec, M. Salvi, H. L'Haridon, and M. Gauneau, "Anomalous behavior of ion-implanted GaSb," *Appl. Phys. Lett.*, 1991, doi: 10.1063/1.106173.

[22] R. Callec, A. Poudoulec, M. Salvi, H. L'Haridon, P. N. Favennec, and M. Gauneau, "Ion implantation damage and annealing in GaSb," *Nucl. Inst. Methods Phys. Res. B*, 1993, doi: 10.1016/0168-583X(93)96175-C.

[23] A. G. Milnes *et al.*, "Ion implantation effects in GaSb," *Mater. Sci. Eng. B*, vol. 27, no. 2–3, pp. 129–136, 1994, doi: 10.1016/0921-5107(94)90133-3.

[24] Y. K. Su, K. J. Gan, J. S. Hwang, and S. L. Tyan, "Raman spectra of Si-implanted GaSb," *J. Appl. Phys.*, vol. 68, no. 11, pp. 5584–5587, 1990, doi: 10.1063/1.346994.

[25] M. V. Rao, A. K. Berry, T. Q. Do, M. C. Ridgway, P. H. Chi, and J. Waterman, "S and Si ion implantation in GaSb grown on GaAs," *J. Appl. Phys.*, vol. 86, no. 11, pp. 6068–6071, 1999, doi: 10.1063/1.371655.

[26] K. S. Jones and C. J. Santana, "Amorphization of elemental and compound semiconductors upon ion implantation," *J. Mater. Res.*, vol. 6, no. 5, pp. 1048–1054, 1991, doi: 10.1557/JMR.1991.1048.

[27] N. Rahimi *et al.*, "Beryllium implant activation and damage recovery study in n-type GaSb," *Physics, Simulation, Photonic Eng. Photovolt. Devices III*, vol. 8981, no. March 2014, p. 89811Q, 2014, doi: 10.1117/12.2040276.

[28] N. Rahimi *et al.*, "Epitaxial and non-epitaxial large area GaSb-based thermophotovoltaic (TPV) cells," *2015 IEEE 42nd Photovolt. Spec. Conf. PVSC 2015*, no. January 2016, 2015, doi: 10.1109/PVSC.2015.7356082.

[29] R. Callec and A. Poudoulec, "Characteristics of implantation-induced damage in GaSb," *J. Appl. Phys.*, vol. 73, no. 10, pp. 4831–4835, 1993, doi: 10.1063/1.354090.

[30] "Solar Simulation - Spectral Irradiance - AM0-AM40 | AM1.5G." [Online]. Available: https://g2voptics.com/solar-simulation/. [Accessed: 23-Oct-2020].

[31] S. Kasap, *Optoelectronics and photonics : principles and practices*. Boston: Pearson, 2013.

[32] G. M. T. Marco Rosa-Clot, *Submerged and Floating Photovoltaic Systems*. Elsevier, 2018.

[33] N. Rahimi *et al.*, "Characterization of surface defects on Be-implanted GaSb," *J. Vac. Sci. Technol. B Microelectron. Nanom. Struct.*, vol. 32, no. 4, 2014, doi: 10.1116/1.4886095.

[34] "The Hall Effect | NIST." [Online]. Available: https://www.nist.gov/pml/nanoscale-device-characterization-division/popular-links/hall-effect/hall-effect. [Accessed: 25-Oct-2020].

[35] "Hall Effect and Sheet Resistance Measurement System - IRASOL." [Online]. Available: http://surface.irasol.com/portfolio/hall-effect-measurement/. [Accessed: 26-Oct-2020].

[36] L. Tang, H. Ye, and J. Xu, "A novel zinc diffusion process for the fabrication of high-performance GaSb thermophotovoltaic cells," *Sol. Energy Mater. Sol. Cells*, vol. 122, pp. 94–98, 2014, doi: 10.1016/j.solmat.2013.11.027.

[37] D. J. Herrera, M. B. Clavel, M. K. Hudait, and L. F. Lester, "Device Characterization of a Sulfur-Implanted p++/p GaSb Photovoltaic Camel Diode," *IEEE J. Photovoltaics*, pp. 1–6, 2020, doi: 10.1109/jphotov.2020.3016615.

[38] R. K. Pandey *et al.*, "Higher electrical activation of ion-implanted Si over S in GaSb epitaxial layers," *Mater. Sci. Semicond. Process.*, vol. 115, no. April, p. 105107, 2020, doi: 10.1016/j.mssp.2020.105107.

[39] J. A. Fellows, "Electrical Activation Studies of Ion Implanted Gallium Nitride," *Air force Inst. Technol.*, 2001.

[40] M. A. Green, "Accurate expressions for solar cell fill factors including series and shunt resistances," *Appl. Phys. Lett.*, vol. 108, no. 8, 2016, doi: 10.1063/1.4942660.